


REVIEW

Open Access



Greenhouse gases Observing SATellite 2 (GOSAT-2): mission overview

Ryoichi Imasu^{1*} , Tsuneo Matsunaga², Masakatsu Nakajima³, Yukio Yoshida², Kei Shiomi³, Isamu Morino², Naoko Saitoh⁴, Yosuke Niwa², Yu Someya², Yu Oishi^{2,6}, Makiko Hashimoto³, Hibiki Noda², Kouki Hikosaka⁵, Osamu Uchino², Shamil Maksyutov², Hiroshi Takagi², Haruma Ishida⁷, Takashi Y. Nakajima⁸, Teruyuki Nakajima³ and Chong Shi⁹

Abstract

The Greenhouse gases Observing SATellite 2 (GOSAT-2) was launched in October 2018 as a successor to GOSAT (launched in 2009), the first satellite to specialize in greenhouse gas observations. Compared to the GOSAT sensors, the sensors of GOSAT-2 offer higher performance in most respects. The quality and quantity of data from observations are expected to be improved accordingly. The signal-to-noise ratio (SNR) is better in both the SWIR and TIR bands of TANSO-FTS-2, which is the main sensor of GOSAT-2. This improvement ultimately enhances the accuracy of greenhouse gas concentration analysis. Furthermore, because of the improved SNR in the SWIR band, the northern limit at which data are obtainable in high-latitude regions of the Northern Hemisphere in winter, where observation data have remained unavailable because of weak signal strength, has moved to higher latitudes. As better data are obtained in greater quantities, progress in carbon cycle research for high-latitude regions is anticipated. Moreover, the improvement of SNR in the TIR band is expected to be considerable. Particularly, the resolutions of the vertical concentration distributions of CO₂ and CH₄ have been improved drastically. The first function introduced for GOSAT-2 that is not in GOSAT is an intelligent pointing mechanism: a cloud area avoidance function using the in-field camera of TANSO-FTS-2. This function can increase the amounts of observation data globally and can improve the accuracy of CO₂ emissions estimation and measurements of uptake intensity. The effects are expected to be strong, especially for the tropics because cumulus clouds are the most common cloud type. The intelligent pointing system can avoid the clouds effectively. Another important benefit of TANSO-FTS-2 is that the wavelength range of Band 3 of SWIR has been expanded for measuring carbon monoxide (CO). Because CO originates from combustion, it is used to evaluate some effects of human activities in urban areas and biomass burning in fields. Particularly, black carbon-type aerosols can be measured by the sub-sensor, TANSO-CAI-2, to assess biomass burning along with CO₂ and CO by TANSO-FTS-2.

Keywords GOSAT-2, GOSAT, Carbon dioxide, Methane, Carbon monoxide, Black carbon, Solar-induced chlorophyll fluorescence, TANSO-FTS-2, TANSO-CAI-2, Intelligent pointing mechanism

*Correspondence:

Ryoichi Imasu

imasu@aori.u-tokyo.ac.jp

Full list of author information is available at the end of the article



© The Author(s) 2023, corrected publication 2023. **Open Access** This article is licensed under a Creative Commons Attribution 4.0 International License, which permits use, sharing, adaptation, distribution and reproduction in any medium or format, as long as you give appropriate credit to the original author(s) and the source, provide a link to the Creative Commons licence, and indicate if changes were made. The images or other third party material in this article are included in the article's Creative Commons licence, unless indicated otherwise in a credit line to the material. If material is not included in the article's Creative Commons licence and your intended use is not permitted by statutory regulation or exceeds the permitted use, you will need to obtain permission directly from the copyright holder. To view a copy of this licence, visit <http://creativecommons.org/licenses/by/4.0/>.

1 Introduction

The Greenhouse gases Observing SATellite (GOSAT), the first satellite dedicated to observing greenhouse gases, was launched in 2009 (Hamazaki et al. 2005; Kuze et al. 2009). It continues to make observations normally. The satellite's main sensor, Thermal And Near infrared Sensor for carbon Observation-Fourier Transform Spectrometer (TANSO-FTS), has observed dry air column average concentrations of carbon dioxide and methane and their upper air concentrations for over a decade. Based on these data, inversion analyses of these gases on a sub-continental scale have been performed (e.g., Takagi et al. 2011), contributing to the improvement of the estimation accuracy of the surface fluxes of the gases. Furthermore, observations of solar-induced fluorescence (SIF), an index related to the activity of terrestrial vegetation, were first conducted (Joiner et al. 2011; Frankenberg et al. 2011a, 2011b). The TANSO-Cloud and Aerosol Imager (CAI), an image sensor onboard the satellite, has begun to analyze land aerosols that include black carbon (e.g., Hashimoto and Nakajima 2017).

Based on these achievements, GOSAT-2, a successor of GOSAT, was launched in October 2018. The signal-to-noise ratio of its main sensor, TANSO-FTS-2, has been improved considerably in both the Short Wavelength InfraRed (SWIR) and Thermal InfraRed (TIR) bands. A new spectral band has been added for observing carbon monoxide (CO). Because GOSAT has the important shortcoming that the probability of contamination caused by clouds is closely attributable to its large instantaneous field of view (IFOV), we adopted a new mechanism called intelligent pointing to concentrate the observation points in the clear sky region.

In addition, two observation directions (forward and backward) became available with CAI-2 to better avoid sun glint areas as CAI suffered from them to perform the cloud detection.

Furthermore, the addition of new spectral channels has improved the accuracy of observations of highly light-absorbing aerosols such as black carbon.

Although GOSAT and GOSAT-2 sensors have large IFOV, they have been accumulating long-term global observation data on greenhouse gas concentrations in the atmosphere. On the other hand, for Orbiting Carbon Observatory-2 (OCO-2) (Crisp et al. 2017) and OCO-3 (Eldering et al. 2019), although the observation period is short, high spatial resolution data have been acquired. Combining such different types of sensors is expected not only to compare detection sensitivities, but also to create data sets with well-defined spatiotemporal resolution. On the other hand, regarding atmospheric pollutants such as black carbon, the synergy between GOSAT and GOSAT-2 on-board sensors with a small

instantaneous field of view and sensors such as The TROPospheric Monitoring Instrument (TROPOMI) (e.g., Torres et al. 2020) and Ozone Monitoring Instrument (OMI) (e.g., Jethva and Torres 2019), which can simultaneously measure many chemical substances and aerosols, is expected to bring more detailed knowledge of atmospheric chemistry.

Chapter 2 of this article presents detailed specifications of satellites and sensors. The data analysis algorithms of TANSO-FTS-2 and CAI-2 are described in Chapter 3. In Chapter 4, calibration of the radiance data observed by sensors and verification of level 2 data such as gas concentration and aerosol content are described. In Chapter 5, the scientific goals related to the global and regional carbon cycles, SIF measurements, and air pollution monitoring using GOSAT sensors are described based on the project's science plan (Imasu 2019).

2 Satellite and sensors

2.1 Satellite bus system

Like its predecessor, GOSAT, the GOSAT-2 (known as "IBUKI-2") satellite is dedicated to the observation of greenhouse gases. It carries two mission instruments that provide higher performance than those of GOSAT: Thermal And Near infrared Sensor for carbon Observation-Fourier Transform Spectrometer-2 (TANSO-FTS-2) ("FTS-2") and Cloud and Aerosol Imager-2 (TANSO-CAI-2) ("CAI-2"). GOSAT-2 is flying in a sun-synchronous sub-recurrent orbit. Based on the operation of GOSAT and the mission requirements for GOSAT-2, some functions and performances have been improved as explained below.

The recurrence cycle of GOSAT is 3 days. The distance to the next orbit is about 900 km on the equator. However, the swath of TANSO-CAI is 1,000 km, so areas lying somewhere between the two orbits are observed with large off-nadir angles, which prevents improvement of the aerosol measurement accuracy. Therefore, it was decided that GOSAT-2 should pass between the GOSAT orbits so that the areas lying somewhere between two GOSAT orbits would be observed with a small off-nadir angle. Furthermore, the recurrence cycle which depends on the orbit height and inclination was set as 6 days. Two candidates of orbit heights and lower height orbit of 613 km were selected because the footprint size of FTS-2 would thereby be smaller. The GOSAT orbit was set in such manner that GOSAT flies over Tsukuba, Japan, where the Total Carbon Column Observing Network (TCCON) can acquire validation data. However, because many data acquired at Tsukuba are contaminated by clouds, the GOSAT-2 orbit was set to fly over another TCCON site, Lamont, where it is possible to anticipate sunny days.

Table 1 Principal specifications of GOSAT-2 compared with GOSAT

Items	GOSAT-2	GOSAT
Main body	5.3 m × 2.0 m × 2.1 m	3.7 m × 1.8 m × 2.0 m
Size	(Wing Span 16.5 m)	(Wing Span 13.7 m)
Total mass	1700 kg	1750 kg
Total power	5.0 kW (EOL)	3.8 kW (EOL)
Life time	Five years	Five years
Orbit	Sun synchronous orbit	Sun synchronous orbit
Local time	13:00 ± 0:15	13:00 ± 0:15
Altitude	613 km	666 km
Inclination	98°	98°
Repeat	6 days (89 revol.)	3 days (44 revol.)



Fig. 1 Artistic image of GOSAT-2 in orbit

In cases where only low power is available, as might occur with the breakdown of one solar array paddle, GOSAT was designed to halt observations in the TIR band of FTS and CAI. By contrast, GOSAT-2, with its larger-sized solar array paddle than that of GOSAT, is designed to continue operations of all mission instruments even after the breakdown of one solar array paddle.

Table 1 and Fig. 1, respectively, present the principal specifications of GOSAT-2 and an artistic image of GOSAT-2 on orbit.

2.2 TANSO-FTS-2

2.2.1 Overview

TANSO-FTS-2 is a Fourier transform spectrometer (FTS), as is TANSO-FTS on GOSAT. The pointing mirror steers the line of sight to the observation area. After the scene flux passes the interferometer, it is divided into five observation bands by the dichroic filters. Additionally, bands other than the TIR are divided into two polarizations: P and S. They form an image on the detectors by the imaging optics. Table 2 presents the principal specifications of the TANSO-FTS-2. Also, Figs. 2, 3, and 4, respectively, present an outline view of the sensor unit of TANSO-FTS-2, a ray diagram, and details of the division of the band.

Table 2 Principal specifications of TANSO-FTS-2 compared with TANSO-FTS

Items	TANSO-FTS-2/GOSAT-2	TANSO-FTS/GOSAT
Measured gases	CO ₂ , CH ₄ , O ₃ , H ₂ O, CO	CO ₂ , CH ₄ , O ₃ , H ₂ O
FOV	15.8 mrad (9.7 km)	15.8 mrad (10.5 km)
Spectral ranges (μm) (cm ⁻¹)	Band 1: 0.75–0.77 (12,950–13,250) Band 2: 1.56–1.69 (5900–6400) Band 3: 1.92–2.33 (4200–5200) Band 4: 5.5–8.4 (1188–1800) Band 5: 8.4–14.3 (700–1188)	Band 1: 0.75–0.77 (12,900–13,200) Band 2: 1.56–1.72 (5800–6400) Band 3: 1.92–2.08 (4800–5200) Band 4: 5.5–14.3 (700–1800)
SNR(@standard radiance)	Band 1: > 400 (P@13,050 cm ⁻¹) Band 2: > 300 (P@6,200 cm ⁻¹) Band 3: > 300 (P@5,000 cm ⁻¹) > 300 (P + S@4,250 cm ⁻¹) Band 4: > 300 (@1,300 cm ⁻¹) Band 5: > 300 (@700 cm ⁻¹)	Band 1: > 300 Band 2: > 300 Band 3: > 300 Band 4: > 300
Observation mesh	160 km (5 points in the CT direction)	160 km (5 points in the CT direction)
Scan duration	4 s/interferogram	4, 2, 1.1 s/interferogram
Sampling resolution	0.2 cm ⁻¹	0.2 cm ⁻¹
Effective aperture size	Φ73 mm	Φ64 mm
Gain steps	16	2
Avoidance of the cloud	Intelligent pointing	–

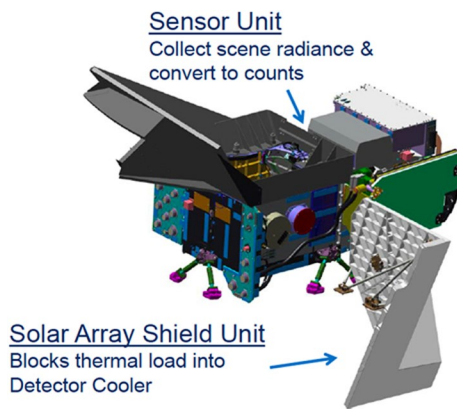


Fig. 2 Outline view of FTS-2 the sensor

2.2.2 Improvements from TANSO-FTS on GOSAT

The increase in signal-to-noise ratio (SNR) and the addition of carbon monoxide measurements were necessary to satisfy mission requirements such as anthropogenic emission estimation over mega cities. Furthermore, the effective aperture size was extended from TANSO-FTS. The band range of the 2.0 μm band was extended to 2.3 μm .

To minimize the change of design from TANSO-FTS to the greatest degree possible, the basic design of the interferometer was retained. The aperture size was extended to the maximum size, which is available with the basic design of TANSO-FTS to increase the signal level. Based

on GOSAT operations and the mission requirements, the spectral range of each band was optimized to decrease the noise level.

The range of each band was changed from that of GOSAT. The range of Band 1 was shifted slightly based on results of GOSAT data utilization. That of Band 2 was reduced to increase SNR by cutting the range which has not been used. That of Band 3 was extended to 2.3 μm to observe the carbon monoxide. TIR band was divided into two bands, Bands 4 and 5, to increase the SNR. Details about SNR for each spectral band are described by Suto et al. (2021, 2022) as a function of radiance intensity. For reference, comparison of SNR of detectors in the same wavenumber range for TANSO-FTS and TANSO-FTS-2 is shown in Tables 2, 3. Basically, apodization processing has not been applied to the spectra of all bands in the retrieval analysis. The IFOV is 15.8 mrad, which is the same as that of GOSAT, but the footprint size was decreased from 10.5 to 9.7 km because of the lower GOSAT-2 altitude.

The Instrument Spectral Response Function (ISRF) is almost same as that of TANSO-FTS on GOSAT. The ISRF was evaluated using the Instrument Line Shape (ILS) target on TANSO-FTS-2, which is an integrated sphere with laser diodes of 768 nm and 1543 nm, respectively, for Bands 1 and 2, and a gas cell on the ground. The ISRFs of Bands 1 and 2 were evaluated on orbit using the ILS target. The FWHMs of Bands 1 and 2 were proved to be maintained at almost the same value as that obtained

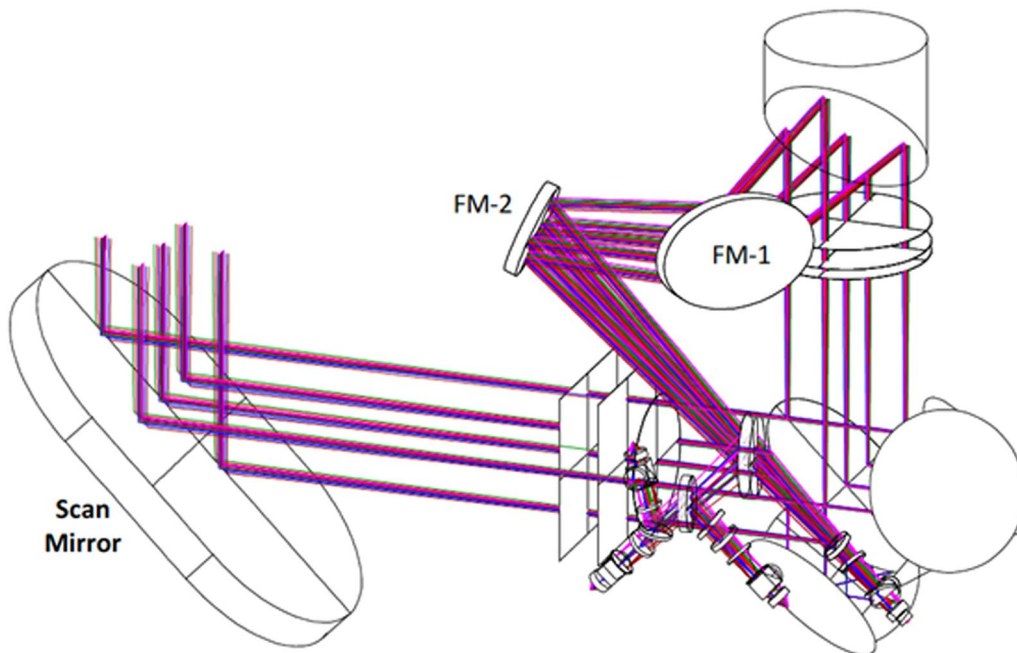


Fig. 3 Ray diagram of TANSO-FTS-2

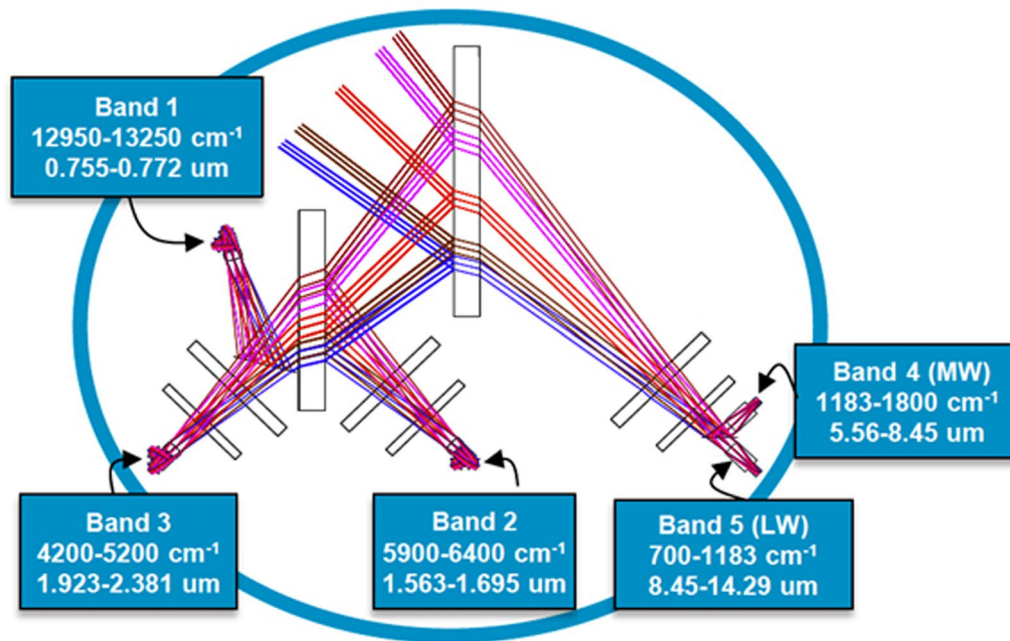


Fig. 4 Details of the division of the band

Table 3 Signal-to-noise ratio (SNR) of detectors of TANSO-FTS-2 and TANSO-FTS (obtained on the ground before satellite launch)

Band	Wavenumber (cm ⁻¹)	TANSO-FTS-2	TANSO-FTS
B1P	13,050	561	345
B1S	13,050	462	247
B2P	6200	459	322
B2S	6200	390	258
B3P	5000	326	412
B3S	5000	252	287
B3P	4250	257	-
B3S	4250	303	-
B4	1300	1512	298
B5	700	941	-

during ground testing by evaluation done for the commissioning phase. The ISRF of Band 2 measured on orbit is shown in Fig. 5.

Except for Band 1, for which the sampling resolution is different from those of other bands, all bands have almost the same FWHM. Details about ILS and its spectral dependences are described by Suto et al. (2021, 2022).

In addition, the pointing angle in the along track direction increased from ± 20 degrees to $\pm 40^\circ$ to extend the sun glint observation area. GOSAT observes the standard mesh points, which are arranged with regularity. Up to 1500 points, a day can be replaced with specific points.

By contrast, GOSAT-2 is capable of observing all points as specific points. One can select the observation points freely within the capabilities of the pointing mirror moving speed.

The observation points are stored in the ground system as an observation table that is assigned to one recurrence cycle of 6 days. The ground system can hold up to five tables. The observation points in the table will be replaced with new specific points such as points required by users including PIs. The table of one-day observation points is uploaded to GOSAT-2: GOSAT-2 can then hold tables for two days. TANSO-FTS on GOSAT can select the scan duration, which is the time to select one interferogram from a menu of choices: 1.1 s, 2 s, and 4 s. However, the SNR of the data taken with the durations of 1.1 s and 2 s is relatively low. Therefore, TANSO-FTS-2 on GOSAT-2 makes observations with only 4 s scan duration. It is difficult to optimize the gain to fit the scene because TANSO-FTS has only two steps of the gain. TANSO-FTS-2 has 16 steps of the gain to take advantage of the dynamic range, accommodating very different radiance.

2.2.3 Intelligent pointing

Although TANSO-FTS with a point detector observes discretely distributed points, any clouds in the scene, however small, render the data invalid. TANSO-FTS-2 has a function of avoiding the clouds in the

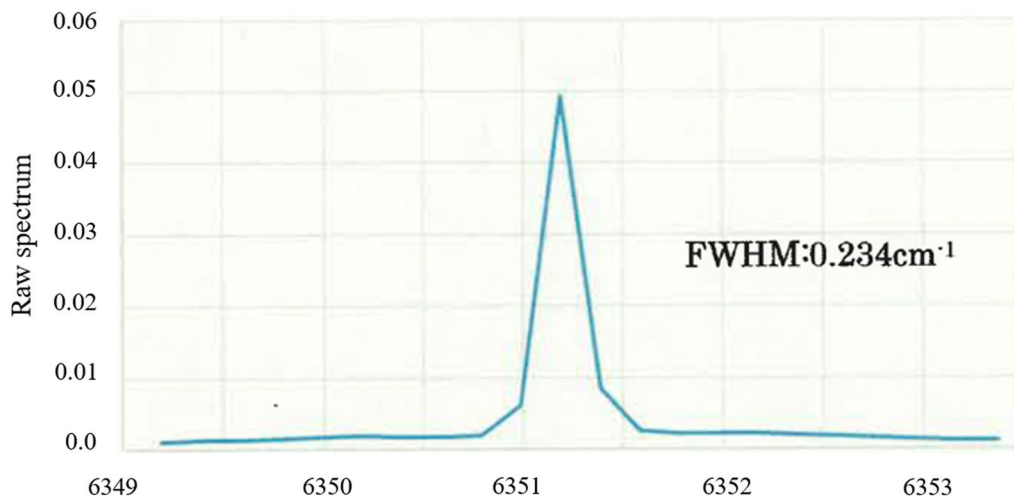


Fig. 5 ISRF of Band 2 measured on orbit

scene. This function operates as follows: The image of an 50 km×30 km area around the planned observation point is obtained using the RGB camera for which the line of sight (LOS) is adjusted coaxially with that of TANSO-FTS-2. Once clouds in the image are detected, the LOS will be shifted to the cloud free area by steering

the pointing mirror. This sequence of actions is completed within about 650 ms turnaround time. A detailed sequence of the intelligent pointing is presented in Fig. 6; also, Fig. 7 presents actual pictures acquired by the monitor camera in orbit. It is possible to switch the intelligent pointing on and off.

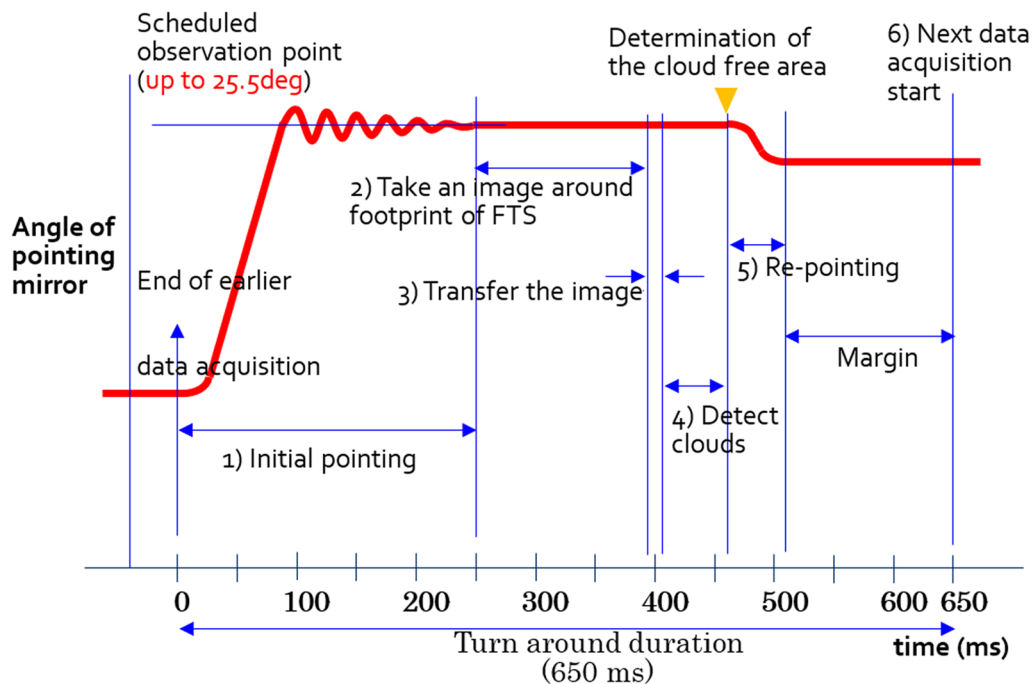


Fig. 6 Detailed sequence of intelligent pointing. After completion of the preceding observation, the line of the sight (LOS) is steered to the next scheduled observation point. After the steering was stopped completely, after about 250 ms of the start of the steering, the image around the scheduled observation point is taken by the monitor camera (about 150 ms duration of). Then, the image is transferred to the processing part; the clouds are detected with about 50 ms duration). Based on these results, the cloud-free area is determined. The LOS is steered to that area (about 50 ms duration of). The next measurement starts at 650 ms after completion of the preceding observation

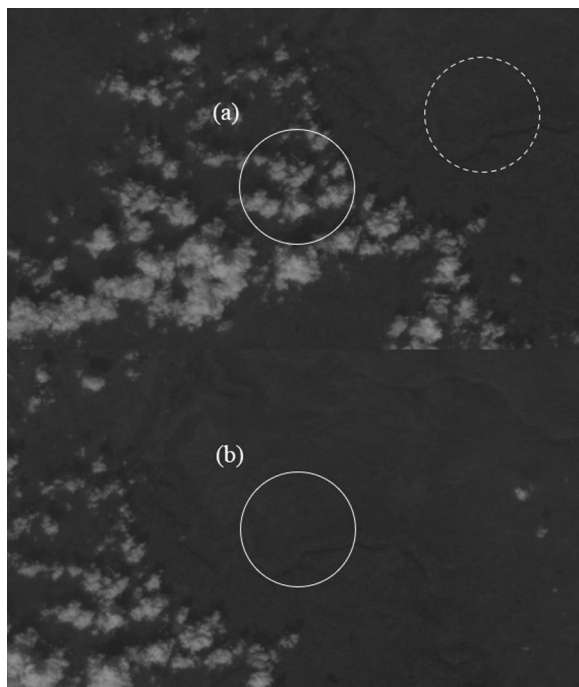


Fig. 7 Images acquired by the monitor camera at the planned steering and after the steering of the LOS. **a** Planned observation point. The solid circle shows the planned observation point. The dotted circle shows the determination of no clouds and shows what can be observed. **b** Actually observed point. This area is the same as that of the dotted circle of **a**

This pointing mechanism including the algorithm was confirmed by trial manufacturing and flight test, combined with a FTS for airplanes. The intelligent mechanism was confirmed to have functioned as expected at about 45% of the approximately 3600 observation points. However, the RGB camera used for this experiment on the airplane had had about one-hundredth of the IFOV of the camera equipped with TANSO-FTS-2. Therefore, cloud detection was easy. For that reason, 45% seems to be larger than the actual FTS-2 case.

According to the simulation using the monitor camera data obtained by TANSO-FTS on GOSAT, the number of valid data is expected to increase to about two times that of GOSAT. The model used for the flight test of the intelligent pointing and photographs taken before and after cloud avoidance are presented, respectively, in Figs. 8 and 9.

2.3 TANSO-CAI-2

TANSO-CAI-2 is a push-broom-type imaging radiometer using a linear array sensor and band pass filter, similarly to TANSO-CAI. The LOS of TANSO-CAI-2 is tilted $\pm 20^\circ$ in the along track direction relative to TANSO-CAI, for which the LOS points to the nadir direction. Also, TANSO-CAI-2 consists of five lens systems. Each lens system has two FOVs of forward and backward viewing.

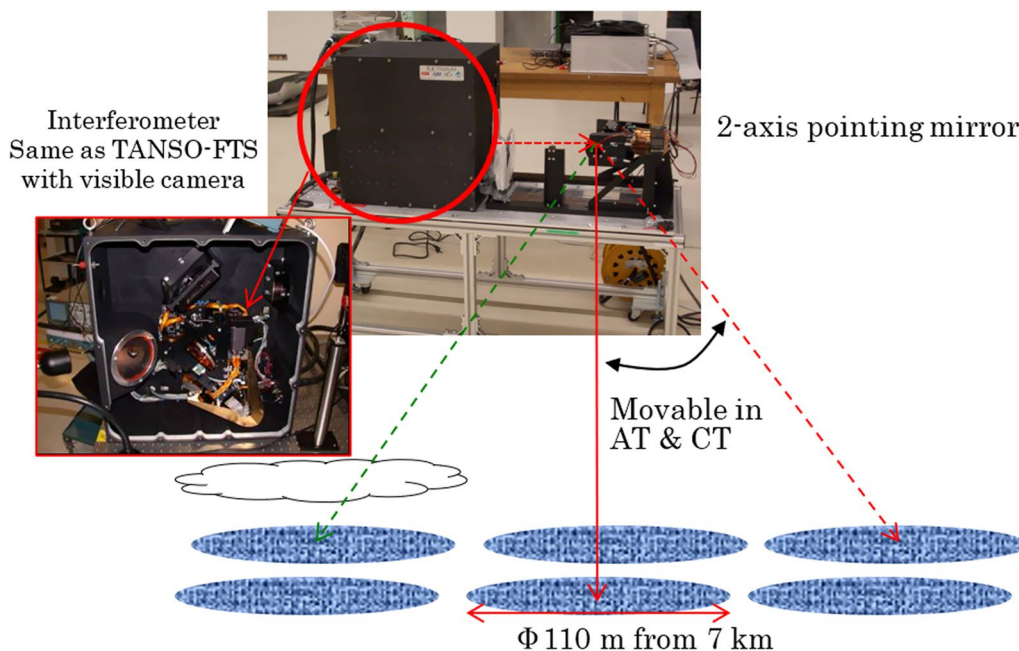


Fig. 8 Model used for flight testing of intelligent pointing

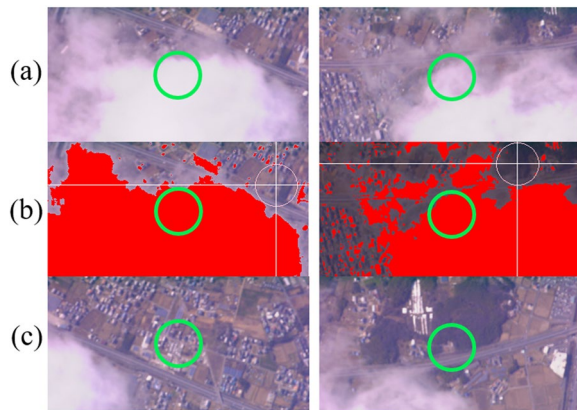


Fig. 9 Photographs taken before and after cloud avoidance for two cases (left and right). Green circle represents observation points. **a** Scheduled pointing, **b** processing the cloud and cloud free area (white circles are scheduled pointing position and red presents the cloud area), and **c** re-pointing to the cloud free area

Based on requirements to improve the measurement accuracy of aerosols, three new observation bands were added to TANSO-CAI-2 in addition to the four observation bands of TANSO-CAI. Furthermore, three bands are available for observation by forward and backward viewings. The swath of the 1.6 μm band of TANSO-CAI is 750 km, which is 25% narrower than other bands. Therefore, the swath of the 1.6 μm band of TANSO-CAI-2 was matched with those of other bands.

Table 4 presents the principal specifications of TANSO-CAI-2. Also, Figs. 10 and 11 depict an outline

view of the sensor unit of TANSO-CAI-2 without insulation, multilayer insulation (MLI), and a cross section of the lens system.

3 Retrieval methods

3.1 TANSO-FTS-2 SWIR

3.1.1 Overview

From TANSO-FTS-2 SWIR Level 2 processing, “TANSO-FTS-2 SWIR L2 Chlorophyll Fluorescence and Proxy-method Product” and “TANSO-FTS-2 SWIR L2 Column-averaged Dry-air Mole Fraction Product” are obtained.

The TANSO-FTS-2 SWIR L2 Chlorophyll Fluorescence and Proxy-method Product includes the six individual retrieval results processed under the assumptions of cloud-free and aerosol-free conditions. Six wavenumber ranges, two each from the three TANSO-FTS-2 SWIR bands, correspond to six independent retrievals. From TANSO-FTS-2 Band 1, data of solar-induced chlorophyll fluorescence (SIF) and surface pressure are retrieved, respectively, using Fraunhofer lines in the wavenumber range, where the O₂ absorption and the O₂ A-band are negligibly small. From TANSO-FTS-2 Band 2, XCO₂ and XCH₄ are retrieved, respectively, from the 1.6 μm CO₂ band and 1.67 μm CH₄ band. From TANSO-FTS-2 Band 3, XCO₂ and XH₂O, and XCO, XCH₄, and XH₂O are retrieved, respectively, using the 2.08 μm CO₂ band and 2.3 μm CO band. SIF is weak radiation emitted by chlorophylls during photosynthesis. It appears as the variation in fractional depth (filling in) of the Fraunhofer

Table 4 Principal specifications of TANSO-CAI-2 compared with TANSO-CAI

Items	TANSO-CAI-2/GOSAT-2	TANSO-CAI/GOSAT
	Forward Viewing (+20°)	Backward Viewing (−20°)
Spectral range (nm)	b 1: 333–353 b 2: 433–453 b 3: 664–684 b 4: 859–879 b 5: 1585–1675	b 6: 370–390 b 7: 540–560 b 8: 664–684 b 9: 859–879 b 10: 1555–1645
Spatial resolution	Except Bands 5, 10 Bands 5, 10	Except Bands 5, 10 Bands 5, 10
(@nadir)	460 m (700 mrad) 920 m (1400 mrad)	500 m (750 mrad) 1500 m (2250 mrad)
Swath (FOV)	920 km	920 km
SNR	b 1: > 200 (45/0.158)	b 6: > 200 (48/0.152)
(@spectral-radiance/albedo)	b 2: > 200 (79/0.144)	b 7: > 200 (65/0.125)
(W/m ² /sr/μm)	b 3: > 200 (46/0.106)	b 8: > 200 (46/0.106)
	b 4: > 200 (30/0.112)	b 9: > 200 (30/0.112)
	b 5: > 200 (7/0.101)	b 10: > 200 (7/0.101)

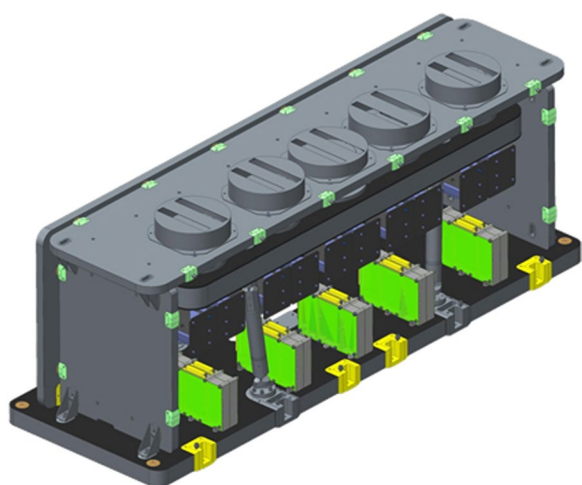


Fig. 10 Outline view of the sensor unit of CAI-2 without MLI

lines in the satellite-observed spectrum. Using this filling-in signal, SIF can be retrieved from satellite observed spectra (Frankenberg et al. 2011a, 2011b). Aside from SIF retrieval, five other retrievals use atmospheric absorption bands. Because these retrievals are processed under the assumption of cloud-free and aerosol-free conditions, the retrieved column-averaged dry-air mole fractions include some effects from optical path length modifications. If the column-averaged dry-air mole fraction of some gas species (X_{gas}) area is obtained with high accuracy using a model-based calculation or other methods, then that gas is useful as an optical path length proxy by comparing the retrieved X_{gas} to prior knowledge. Because the degree of optical path length modification is regarded as similar to

the nearby wavelength, the evaluated optical path length proxy is then useful to target gas retrieval. This method is designated as a “proxy method.” The CO_2 retrieved from the $1.6\ \mu m$ CO_2 band is often used as the optical path length proxy to obtain XCH_4 from the $1.67\ \mu m$ CH_4 band (e.g., Frankenberg et al. 2011a, 2011b; Parker et al. 2011). Furthermore, the difference between the retrieved and a priori values of surface pressure obtained under the assumption of cloud-free and aerosol-free conditions is expected to reflect the degree of optical path length modification because of clouds and aerosols. Therefore, the TANSO-FTS-2 SWIR L2 Chlorophyll Fluorescence and Proxy-method Product includes retrieval results for all TANSO-FTS-2 SWIR observations.

The TANSO-FTS-2 SWIR L2 Column-averaged Dry-air Mole Fraction Product includes simultaneously retrieved XCO_2 , XCH_4 , XH_2O , and XCO considering clouds and aerosols and using the several wavenumber ranges. This retrieval is designated as the “full-physics method” after the mode of the treatment of the optical path length modification. In the full-physics method, the optical path length modification attributable to clouds and aerosols is described by atmospheric scattering processes using the forward model. Being different from the proxy method, the full-physics method has the important benefit that no limitation exists for the gas species to retrieve. However, its retrieval error depends strongly on how accurately the forward model can represent the optical path length modifications attributable to clouds and aerosol scattering. Therefore, TANSO-FTS-2 SWIR observations that are affected strongly by clouds and/or aerosols are not processed using the full-physics method.

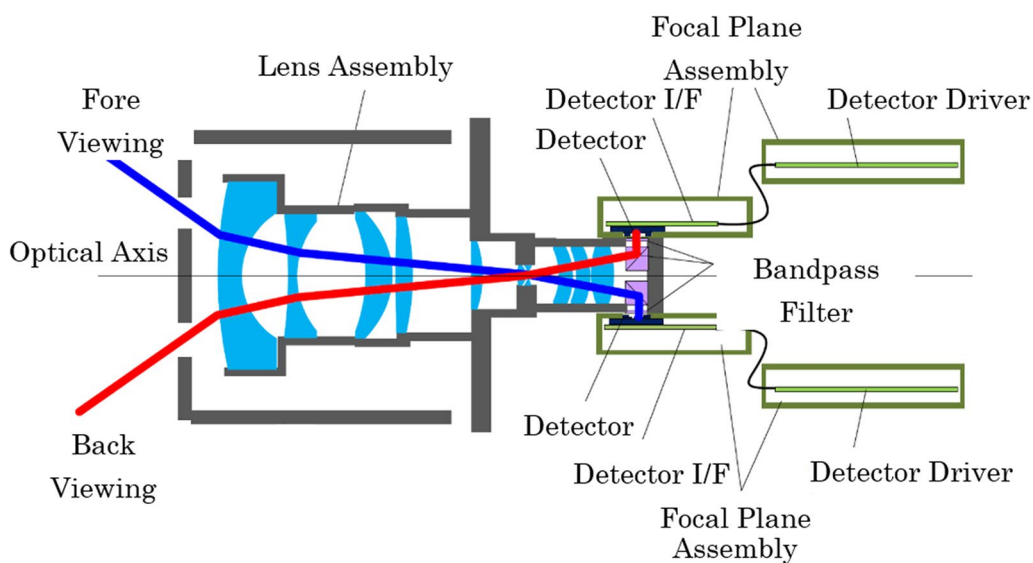


Fig. 11 Cross section of the lens system

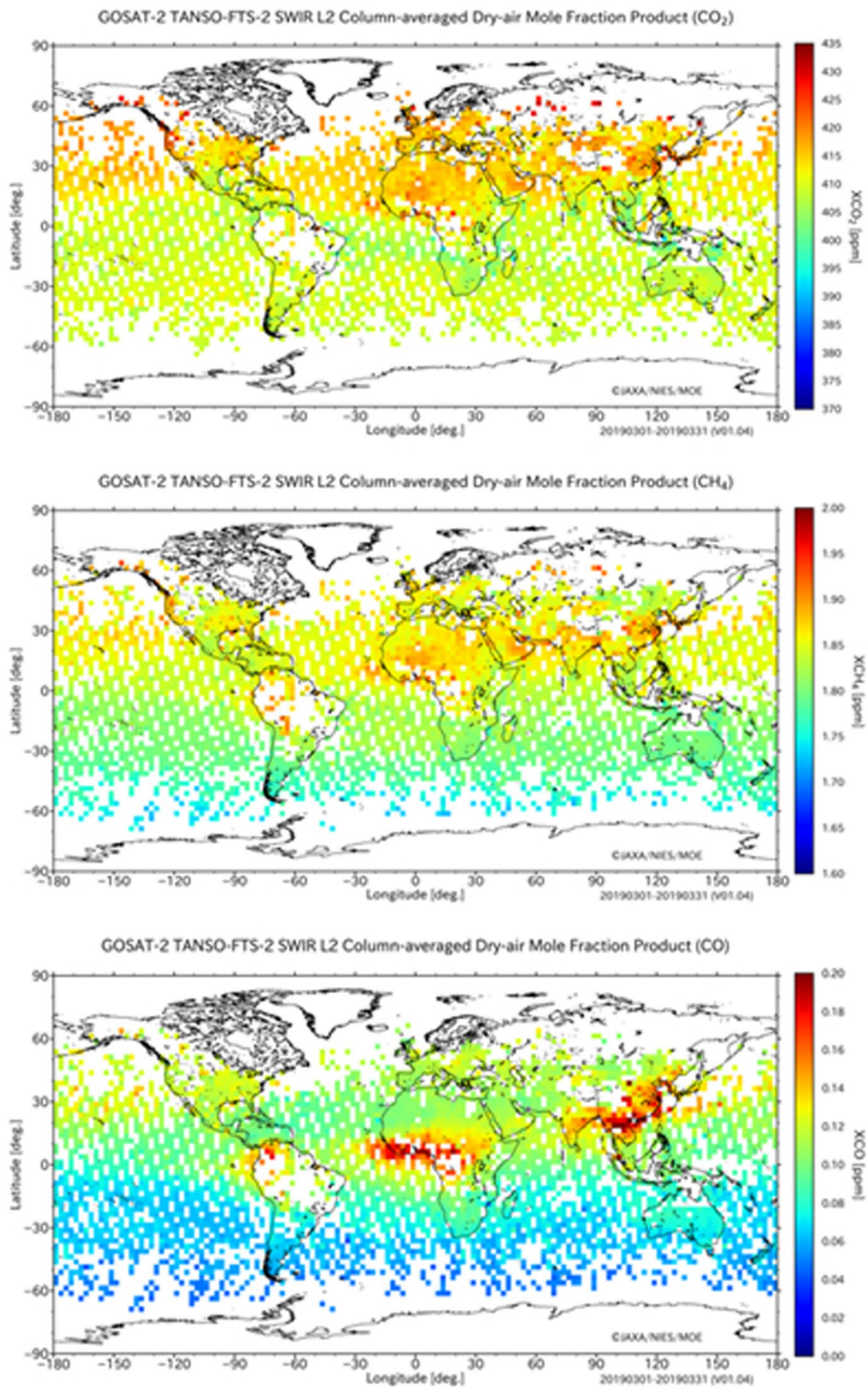


Fig. 12 Examples of column-averaged dry-air mole fraction products of CO₂ (top), CH₄ (middle), and CO (bottom). The product data version is V01.07. Values are averaged in each 2.5° mesh area for March 2019

Retrieval results for converged cases in the retrieval processing are stored in the TANSO-FTS-2 SWIR L2 Column-averaged Dry-air Mole Fraction Product.

Differences in the wavenumber range of observed spectra, state vector elements, and treatment of clouds and aerosols can be treated as differences in retrieval settings. The Maximum A Posteriori (MAP) retrieval method (Rodgers 2000) is used for all retrieval processing.

Figure 12 presents examples of column-averaged dry-air mole fraction products of CO₂, CH₄, and CO as averaged values in each 2.5° mesh area for March 2019.

3.1.2 Maximum posterior (MAP) analysis method

According to the MAP analysis method, the optimal estimate of state vector \mathbf{x} , which represents unknown parameters to be retrieved, is the value of \mathbf{x} which minimizes cost function $J(\mathbf{x})$, as expressed in Eq. (1).

$$J(\mathbf{x}) = [\mathbf{y} - \mathbf{F}(\mathbf{x}, \mathbf{c})]^T \cdot \mathbf{S}_\varepsilon^{-1} \cdot [\mathbf{y} - \mathbf{F}(\mathbf{x}, \mathbf{c})] + (\mathbf{x} - \mathbf{x}_a)^T \cdot \mathbf{S}_a^{-1} \cdot (\mathbf{x} - \mathbf{x}_a) \quad (1)$$

Therein, \mathbf{y} represents the observed radiance spectrum, $\mathbf{F}(\mathbf{x}, \mathbf{c})$ denotes a forward model, i.e., the spectrum computed with the state vector \mathbf{x} and other necessary variables \mathbf{c} as inputs, \mathbf{x}_a is the a priori state vector, \mathbf{S}_a represents the variance–covariance matrix of \mathbf{x}_a , and \mathbf{S}_ε is the variance–covariance matrix of observation error and forward model.

In TANSO-FTS-2 SWIR L2 processing, solution \mathbf{x} is obtained iteratively from Eq. (2).

$$\mathbf{x}_{i+1} = \mathbf{x}_i + \left(\mathbf{K}_i^T \cdot \mathbf{S}_\varepsilon^{-1} \cdot \mathbf{K}_i + \mathbf{S}_a^{-1} + \lambda \cdot \mathbf{D}^2 \right)^{-1} \cdot \left\{ \mathbf{K}_i^T \cdot \mathbf{S}_\varepsilon^{-1} \cdot [\mathbf{y} - \mathbf{F}(\mathbf{x}_i)] - \mathbf{S}_a^{-1} \cdot (\mathbf{x}_i - \mathbf{x}_a) \right\} \quad (2)$$

In that equation, subscript i denotes the number of iterations, $\mathbf{K} = \partial \mathbf{F}(\mathbf{x}) / \partial \mathbf{x}$ is a Jacobian, \mathbf{D} is a diagonal matrix introduced to stabilize the iteration process, and λ represents a coefficient of which the value is adjusted so that the value of the cost function decreases in each step of the iteration.

Here, the posterior error covariance matrix \mathbf{S} and the averaging kernel matrix \mathbf{AK} are given, respectively, by Eqs. (3) and (4).

$$\mathbf{S} = \left(\mathbf{K}^T \cdot \mathbf{S}_\varepsilon^{-1} \cdot \mathbf{K} + \mathbf{S}_a^{-1} \right)^{-1} \quad (3)$$

$$\mathbf{AK} = \left(\mathbf{K}^T \cdot \mathbf{S}_\varepsilon^{-1} \cdot \mathbf{K} + \mathbf{S}_a^{-1} \right)^{-1} \mathbf{K}^T \cdot \mathbf{S}_\varepsilon^{-1} \cdot \mathbf{K} \quad (4)$$

As described earlier, the elements of state vector \mathbf{x} and the wavenumber range of the observed spectrum \mathbf{y} change for each retrieval process, but the same a priori values are used for each type of state vector element (Table 5). The column-averaged dry-air mole fraction of target gas species X_x is obtained by the vertical weighted integral of the gas concentration profile \mathbf{x}_x obtained using MAP analysis (Eqs. 5 and 6). Here, subscript x denotes the elements corresponding to the gas species to be retrieved. To describe the gas concentration profile, we use the layer-averaged (partial column-averaged) dry-air mole fraction of a gas species in a vertical grid that evenly divides the atmosphere by atmospheric pressure.

$$X_x = \mathbf{h}^T \cdot \mathbf{x}_x \quad (5)$$

$$(\mathbf{h})_j = h_j = \frac{w_{dry,j}}{\sum_j w_{dry,j}} \quad (6)$$

Table 5 A priori value of state vector for TANSO-FTS-2 SWIR L2 processing

State vector elements	A priori value	Note
CO ₂ profile	NICAM-TM simulated value	Partial column-averaged dry-air mole fraction
CH ₄ profile	NICAM-TM simulated value	Partial column-averaged dry-air mole fraction
H ₂ O profile	JRA-55 reanalysis value	Partial column-averaged dry-air mole fraction
CO profile	MOZART climatological value	Partial column-averaged dry-air mole fraction
Aerosol profile	SPRINTARS simulated value	Optical thickness
Surface pressure	JRA-55 reanalysis value	
SIF	Zero	
Surface albedo	Calculated from maximum value of the observed radiance under the assumption of Lambert surface with no-scattering and no-absorption atmosphere	For land surface case
Wind speed	JRA-55 reanalysis value	For water surface case

Therein, subscript j denotes a vertical grid; also, w_{dry} is a partial column amount of dry air.

The posterior error σ_x^2 , column averaging kernel \mathbf{a}_x , and degrees of freedom for signals (DFS) with respect to X_x (DFS_x) are given, respectively, by Eqs. (7–9).

$$\sigma_x^2 = \mathbf{h}^T \cdot \mathbf{S}_{xx} \cdot \mathbf{h} \tag{7}$$

$$(\mathbf{a}_x)_j = a_{x,j} = \left(\mathbf{h}^T \cdot \mathbf{AK}_{xx} \right)_j \cdot \frac{1}{h_j} \tag{8}$$

$$DFS_x = \text{trace}(\mathbf{AK}_{xx}) \tag{9}$$

In those equations, \mathbf{S}_{xx} and \mathbf{AK}_{xx} , respectively, represent the sub-matrices of \mathbf{S} and \mathbf{AK} , with regard to the retrieved gas species.

3.1.3 Pre-launch evaluation results based on the designed value of TANSO-FTS-2

Compared to TANSO-FTS, TANSO-FTS-2 SWIR bands show higher SNR values. Its spectral coverage is expanded and optimized for CO and SIF observation (Table 6). This section presents our investigation of the effects of these differences in TANSO-FTS-2 SWIR design on the posterior error (Eq. 7), a column averaging kernel (Eq. 8), and DFS (Eq. 9).

Table 6 Spectral coverage and SNR of SWIR bands of TANSO-FTS and TANSO-FTS-2

TANSO-FTS	Band 1	Band 2	Band 3
Spectral coverage [cm ⁻¹]	12,900–13,200	5800–6400	4800–5200
SNR	343	316	410
Spectral coverage [cm ⁻¹]	12,950–13,250	5900–6400	4200–5200
SNR	562	509	379

The SNR is defined under the diffusive reflectivity of 0.3 and the solar zenith angle of 30°. The SNR of TANSO-FTS is the value in the final performance test. The SNR of TANSO-FTS-2 is the designed value

Table 7 Setting of pre-launch evaluation condition

	Case 1	Case 2	Case 3
Target gas species	CO ₂ , CH ₄ , H ₂ O	CO ₂ , CH ₄ , H ₂ O	CO ₂ , CH ₄ , H ₂ O, CO
Wavenumber range for retrieval [cm ⁻¹]	12,950–13,200 6180–6380 5900–6150 4800–4900	12,950–13,200 6180–6380 5900–6150 4800–4900	12,950–13,200 (O ₂) 6180–6380 (CO ₂ , H ₂ O) 5900–6150 (CH ₄ , H ₂ O) 4800–4900 (CO ₂ , H ₂ O) 4200–4300 (CH ₄ , H ₂ O, CO)
SNR condition	TANSO-FTS final performance test	TANSO-FTS-2 designed value	TANSO-FTS-2 designed value

Gas with an absorption band within the wavenumber range is shown in the column of case 3

For the evaluation, the three cases shown in Table 7 are considered. The effectiveness of the improved SNR and spectral coverage is evaluated, respectively, by comparing cases 1 and 2, and cases 2 and 3. To make the comparison conditions uniform, the actual observation geometric conditions of TANSO-FTS are used; also, the state vector elements and a priori values used to derive the TANSO-FTS- SWIR L2 product version 02 (Yoshida et al. 2011, 2013) are used. However, the variance–covariance matrix \mathbf{S}_a for the a priori value of the gas profile is a diagonal matrix. Also, the diagonal elements are set as (10%)² for CO₂, CH₄, and H₂O, and (100%)² for CO. Furthermore, the variance–covariance matrix for observation error \mathbf{S}_e is a diagonal matrix. For simplicity, its diagonal elements are assumed to consist only of shot noise, which is proportional to the square root of the total number of photons incident on the detector. Under these conditions, evaluation is conducted using 15,751 observation geometric conditions of TANSO-FTS in January, April, July, and October 2011.

Figure 13 presents an example of the averaging kernel matrix (Eq. 4) and the column averaging kernel (Eq. 8). The averaging kernel matrix and the column averaging kernel, respectively, represent the sensitivity of the retrieved profile and X_{gas} to the actual (“true”) profile of target gas. With the improvement of SNR (cases 1 and 2) and the expansion of the wavenumber range (cases 2 and 3), the averaging kernel matrix is changed, but its effect on the column averaging kernel is small. As the SNR improves, the column averaging kernel tends to approach unity, albeit slightly. In any case, the column averaging kernel shows a value that is close to unity over the whole atmospheric layer, indicating that it has sufficient sensitivity to X_{gas} .

Figure 14 portrays histograms of DFS and posterior error. With the improvement of SNR and the expansion of the wavenumber range, DFS increases and posterior error decreases. Regarding XCO₂, almost no difference exists between cases 2 and 3 because the wavenumber range added to case 3 does not include

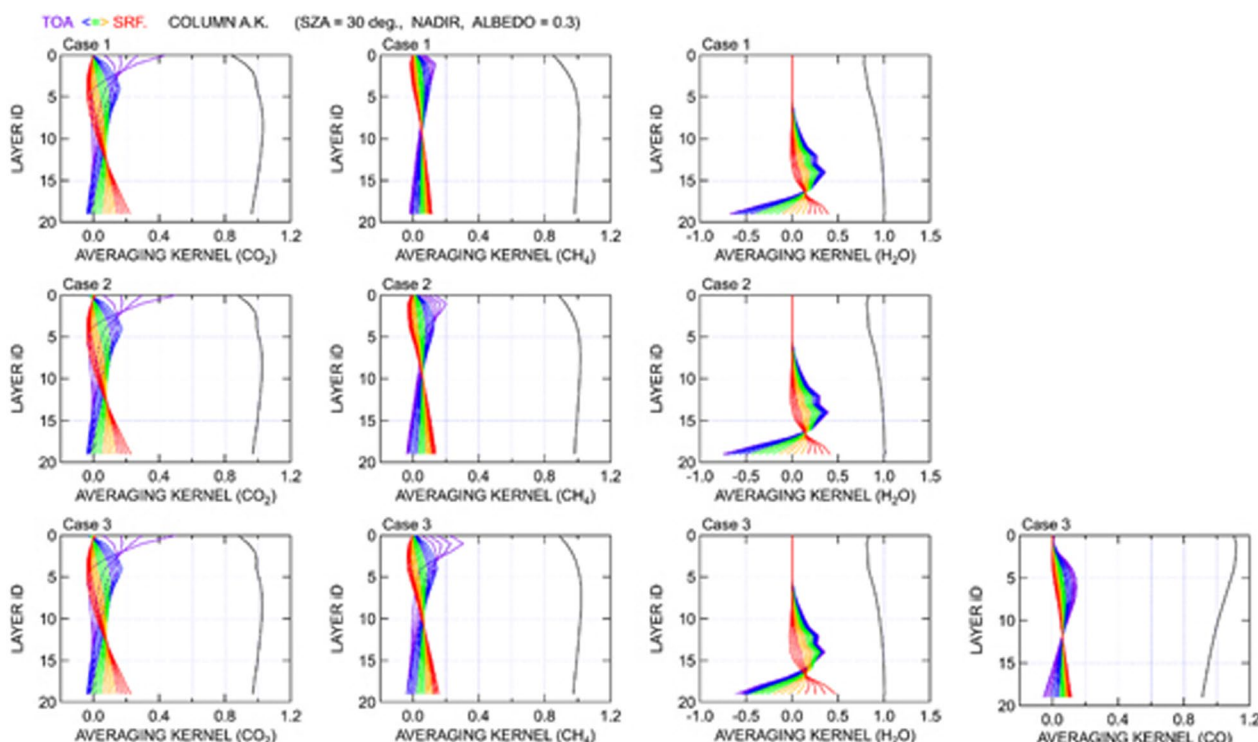


Fig. 13 Example of the averaging kernel matrix (colored lines) and the column averaging kernel (black line). They are calculated under the diffusive reflectivity of 0.3 and the solar zenith angle of 30°. It corresponds to cases 1, 2, and 3 from the top, and CO₂, CH₄, H₂O, and CO from the left. The vertical axis corresponds to the layer number of the atmospheric layer. It is counted from the top-of-the-atmosphere toward the surface. Colors of the averaging kernel matrix also correspond to the layer number of the atmospheric layer, in the order of purple (top-of-the-atmosphere), blue, green, orange, and red (surface)

the CO₂ absorption band. Because DFS exceeds unity in most cases, it can be confirmed that the design result of TANSO-FTS-2 has performance that is sufficient for retrieving X_{gas} . The improvement of SNR contributes greatly to reduction of the posterior error. The posterior errors of X_{CO_2} , X_{CH_4} , and X_{H_2O} are suppressed, respectively, to about 0.85, 0.55, and 0.80 times for GOSAT-2 (case 3) compared to GOSAT (case 1). However, because this evaluation is based on the designed value of TANSO-FTS-2, there is a simplified aspect to the evaluation. It is appropriate to regard it as a result obtained under ideal conditions. It is necessary to make a more realistic evaluation using actual characteristics of TANSO-FTS-2.

3.2 TANSO-FTS-2 TIR

3.2.1 Greenhouse gases and temperature

We have adopted a nonlinear MAP method with linear mapping (Rodgers 2000) to retrieve vertical profiles of greenhouse gases and temperature from the thermal infrared (TIR) bands (Bands 4 and 5) of TANSO-FTS-2 on GOSAT-2, as is true also for the operational data processing of the data of TANSO-FTS on GOSAT (Saitoh et al. 2009, 2016). Regarding retrieval, we have

introduced linear mapping between vertical layer grids for radiative transfer calculation (full grids) and grids for retrieval calculation (retrieval grids). The retrieval grids, which are defined as a subset of the full grids, are fixed for all retrieval processing.

The main target gases of the TIR bands of TANSO-FTS-2 are CO₂, CH₄, H₂O, O₃, and N₂O. Vertical profiles of CO₂, O₃, and temperature are retrieved simultaneously from TIR Band 5 spectra at around 15 μm (690–750 cm⁻¹ and 790–795 cm⁻¹), 10 μm (930–990 cm⁻¹), and 9 μm (1040–1090 cm⁻¹) absorption bands. Vertical profiles of CH₄, H₂O, and N₂O are retrieved simultaneously from TIR Band 4 and 5 spectra at around 7 μm and 8 μm absorption bands (1140–1370 cm⁻¹).

A priori and initial values of meteorological parameters (temperature and water vapor) and the ozone field used in TIR retrieval were referred from the Japan Meteorological Agency (JMA) Japanese 55-year Reanalysis (JRA-55). Profiles of a priori and initial concentrations of CO₂ and CH₄ were taken from outputs of the Non-hydrostatic Icosahedral Atmospheric Model (NICAM)-based Transport Model (TM) (Niwa et al. 2011), which are the same as those used for SWIR retrieval. Profiles

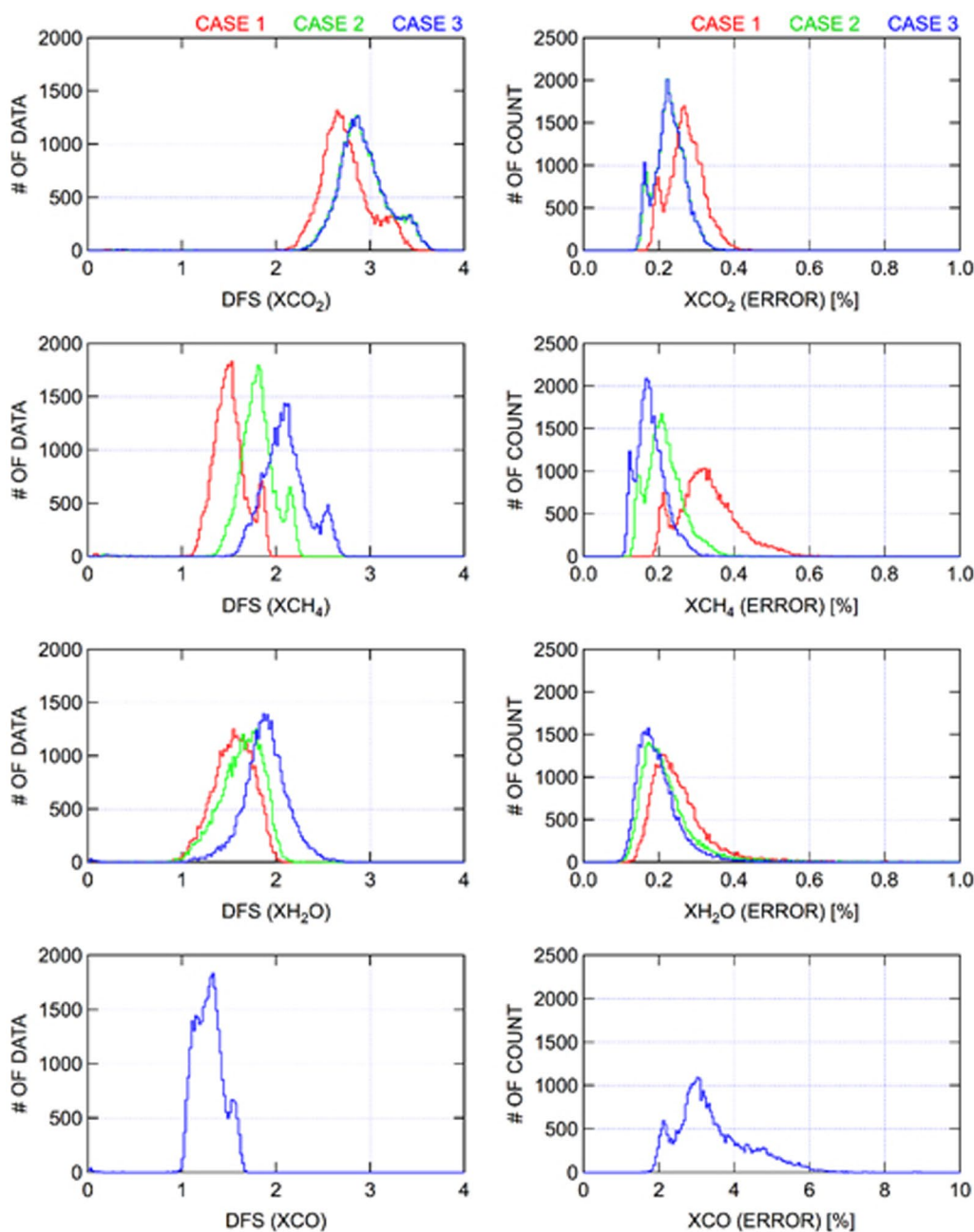


Fig. 14 Histograms of the DFS (left) and posterior error (right) for 15,751 cases in January, April, July, and October 2011. They corresponds to XCO₂, XCH₄, XH₂O, and XCO from the top

of a priori and initial concentrations of N₂O are taken from outputs of the *Atmospheric* Chemistry Transport Model (ACTM) (Ishijima et al. 2010). A priori covariance matrices for these target parameters are set as diagonal matrices with fixed values as elements throughout a vertical profile. Similarly to GOSAT, variation with a standard deviation of approximately 2.5% for CO₂ is assumed for an entire vertical profile (Saitoh et al. 2016). For TIR

retrieval, we used the Line-By-Line Radiative Transfer Model (LBLRTM) (Clough et al. 2005) and the High-resolution Transmission Molecular Absorption Database (HITRAN) (Rothman et al. 2005, 2009, 2013) for line-by-line calculations of optical thickness for each atmospheric layer of the full grids.

Figure 15a shows typical averaging kernel functions (Rodgers 2000) of CO₂ and CH₄ retrievals from

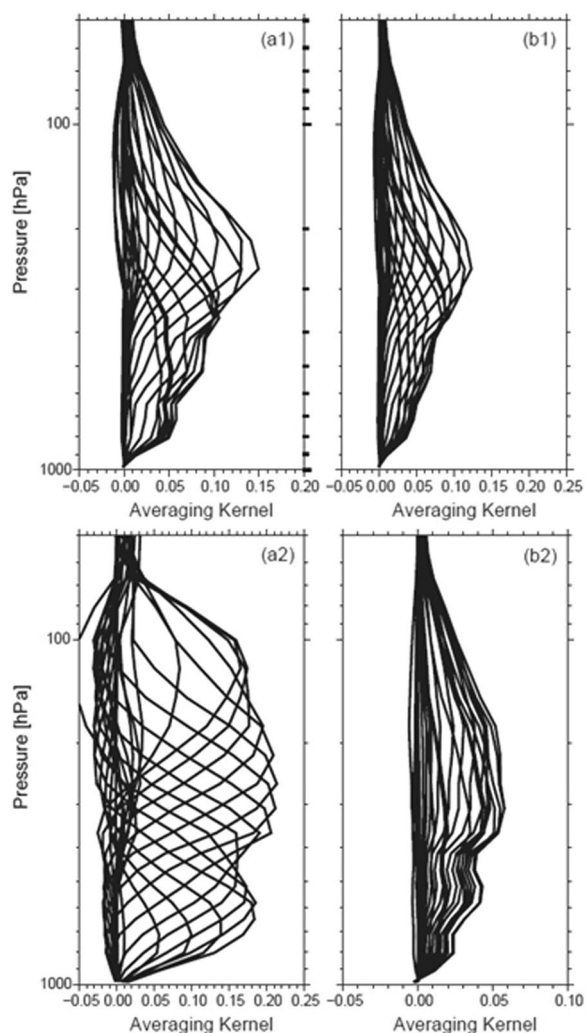


Fig. 15 a Averaging kernel functions of GOSAT-2/TANSO-FTS-2 TIR (left) and those of GOSAT/TANSO-FTS TIR (right). Upper panels show results for CO₂; lower panels show results for CH₄. All functions are calculated under the same atmospheric conditions

TANSO-FTS-2 TIR spectra for atmospheric conditions at low latitudes. For calculating the averaging kernels, we have assumed signal-to-noise ratio (SNR) values for Bands 4 and 5 of TANSO-FTS-2, which were evaluated at the TANSO-FTS-2 Critical Design Review (CDR). The CO₂ and CH₄ averaging kernel functions for the TANSO-FTS TIR band calculated under the same atmospheric conditions are depicted in Fig. 15b for reference. As depicted in Fig. 15, the TANSO-FTS-2 TIR spectra include more information related to CO₂ and CH₄ concentrations than TANSO-FTS. The much higher sensitivity to CH₄ concentration of TANSO-FTS-2 is attributable to the high SNR values of TANSO-FTS-2 Band 4 (1045 at 1300 cm⁻¹).

3.2.2 Other minor constituents

Other than the main targets presented in Sect. 3.2.1, several species have absorption bands in spectral regions from 700 to 1800 cm⁻¹ obtained from Band 4 and 5 of TANSO-FTS-2. The species which might be retrieved from TANSO-FTS-2 are isotopologues of water vapor (HDO and H₂¹⁸O), nitric acid (HNO₃), ammonia (NH₃), methanol (CH₃OH), formic acid (HCOOH), ethene (C₂H₄), peroxyacetyl nitrate (PAN), isoprene (C₅H₈), sulfur dioxide (SO₂), trichlorofluoromethane (CFC-11), and dichlorofluoromethane (CFC-12). The species (except to CFCs) had been retrieved from past and current spaceborne nadir-viewing TIR sounders (e.g., Beer et al. 2008; Coheur et al. 2009). The products available from one of the sounders, Infrared Atmospheric Sounding Interferometer are listed in Clerbaux et al. (2009). HDO (Boesch et al. 2013; Ohyama et al. 2013) and ammonia (Someya et al. 2020) were retrieved from TIR spectra measured by TANSO-FTS on GOSAT.

The abundances of the species are much less than the main absorbers (H₂O, CO₂, CH₄, and O₃). Moreover, their absorption signals are generally weaker than those of the main absorbers. Retrievals of the species are subject to interference from these absorbers and from atmospheric temperature, surface temperature, and surface emissivity because of the overlaps of the absorption bands and water vapor continuum. Therefore, the retrievals must incorporate consideration of these influences. The retrieval algorithms used for earlier studies particularly addressing the species are typically based on the MAP solution (Rodgers 2000), which is spectral fitting using the Bayesian theorem, similar to that used for greenhouse gases. In these algorithms, the interferences are retrieved simultaneously or separately retrieved in advance to input the results into the retrieval of the main target. Because of weak absorption and interference, the information contents of the minor species within the observed spectra are small; also, the retrievals have low ability to resolve vertical profiles. In fact, TANSO-FTS-2 has the highest spectral resolution among the current operating space-borne nadir-viewing TIR sounders, with an SNR much higher than that of TANSO-FTS (Suto et al. 2021, 2022). Therefore, the information contents and the abilities to resolve vertically for the species are expected to be enhanced greatly by TANSO-FTS-2.

3.2.3 Clouds and aerosols

The cloud screening process is important for analyzing gas components such as CO₂. For analysis of the TANSO-FTS-2 (SWIR) band data, the cloud flag of CAI-2 and the cloud information obtained from the SWIR band data

itself are used together. Similarly, for analysis of TANSO-FTS-2 (TIR) band data, the cloud flag of CAI-2 and the cloud information obtained from the TIR band data itself are used together. However, because CAI-2 is not operated during nighttime, the cloud information obtained from the TIR data itself will be used alone.

For cloud screening based on the TIR band data, independent methods of three types are used together. The first is the threshold method for brightness temperature. In this case, when the value of the difference between the observed brightness temperature and the ground surface temperature in the atmospheric window region exceeds a certain threshold value, it is identified that the field of view is covered with clouds. At this time, meteorological analysis data are used as the ground surface temperature, but the surface emissivity estimated from data such as the vegetation index and snow and ice occupancy in the field obtained from MODIS data is used. For this method, the cloud top temperature and height in the field of view are derived as products.

The second method is a slicing method using a CO₂ absorption band. Here, the method described by Someya et al. (2016) is used, which employs a pseudo-spectral channel re-constructed by combining spectral channels having the same peak altitude of the weighting function. In addition to clouds, this method can detect optically thick aerosol layers such as yellow sands (Someya et al. 2019). Using this method, the cloud top height in the field of view is derived as a product.

The third method is the so-called split window method proposed by Inoue (1985). Using this method, the cloud top temperature, the effective cloud particle size, thermodynamic phase of the particles, and their optical thicknesses are derived as products.

3.3 TANSO-CAI-2

3.3.1 Cloud discrimination

The presence of clouds in the instantaneous field of view (IFOV) of the TANSO-FTS-2 engenders incorrect estimates of greenhouse gas concentrations. Consequently, an important role of TANSO-CAI-2 is to perform cloud discrimination to identify and reject cloud-contaminated TANSO-FTS-2 data. Improving the cloud discrimination accuracy necessitates refinement of the existing cloud discrimination algorithm for TANSO-CAI on GOSAT: the CLOUD and Aerosol Unbiased Decision Intellectual Algorithm used with CAI (CLAUDIA1-CAI) (Ishida and Nakajima 2009). A new cloud discrimination algorithm (CLAUDIA3) using a support vector machine (SVM) (Vapnik and Lerner 1963) was developed (Ishida et al. 2018). Primary verification results show that the accuracy of CLAUDIA3-CAI is greater than that of CLAUDIA1-CAI (Oishi et al. 2016). CLAUDIA3-CAI is in the

improvement stage because difficulties to be resolved were also given in the article. A summary of CLAUDIA3-CAI is presented below.

CLAUDIA1 performs cloud discrimination using thresholds that are set based on experience. CLAUDIA3 uses SVM to decide the thresholds objectively using multivariate analysis. SVM is a supervised pattern recognition method using TANSO-CAI-2 Bands 3–5 (forward) or Bands 8–10 (backward).

First, it determines the following items using training samples of typical clear and cloudy pixels: (1) a decision function to discriminate between two classifications (clear and cloudy), (2) the thresholds, and (3) the support vectors, which are training samples specified by the decision function. The support vectors are decided in a high-dimensional feature space of the training samples. Next, it performs cloud discrimination using the decision function, thresholds, and support vectors it determined. The flow of CLAUDIA3-CAI is depicted in Fig. 16. The results are expressed as integrated clear-sky confidence levels (integrated-CCL). Integrated-CCL of 0 expresses that the pixel is cloudy; 1 signifies that the pixel is cloud-free. Ambiguous pixels between cloudy and cloud-free are described using numerical values from 0 to 1. For CLAUDIA3-CAI, the integrated-CCL of 0.5 corresponds to the separating hyperplane of clear support vectors and cloudy support vectors (Oishi et al. 2017, 2018).

Users can adjust the boundaries which separate cloud and clear-sky areas with the integrated-CCL thresholds. They can also discriminate the presence of clouds. Figure 17 presents examples of an input CAI Level 1B product image and its cloud discrimination result obtained using CLAUDIA3-CAI.

TANSO-CAI-2 has forward- (+20°) and backward-looking (−20°) bands. Because cloud discrimination will be performed in each direction, the difference between forward-looking and backward-looking bands of cloud discrimination has been discussed (Oishi et al. 2017, 2018). The use of the forward and backward cloud discrimination during processing for calculating greenhouse gas concentrations (Oishi et al. 2015) is examined.

3.3.2 Aerosol products

TANSO-CAI-2 takes two-directional observations in forward and backward directions. Ten observation bands and seven wavelengths exist, as presented in Table 3. The spatial resolution (IFOV) is 920 m at a 1630 nm wavelength; it is 460 m at the other wavelengths. Actually, TANSO-CAI-2 is characterized by having two wavelengths in the ultraviolet (UV) region of 340 nm and 380 nm that are sensitive to aerosol light absorption characteristics. Therefore, the retrieval accuracy of

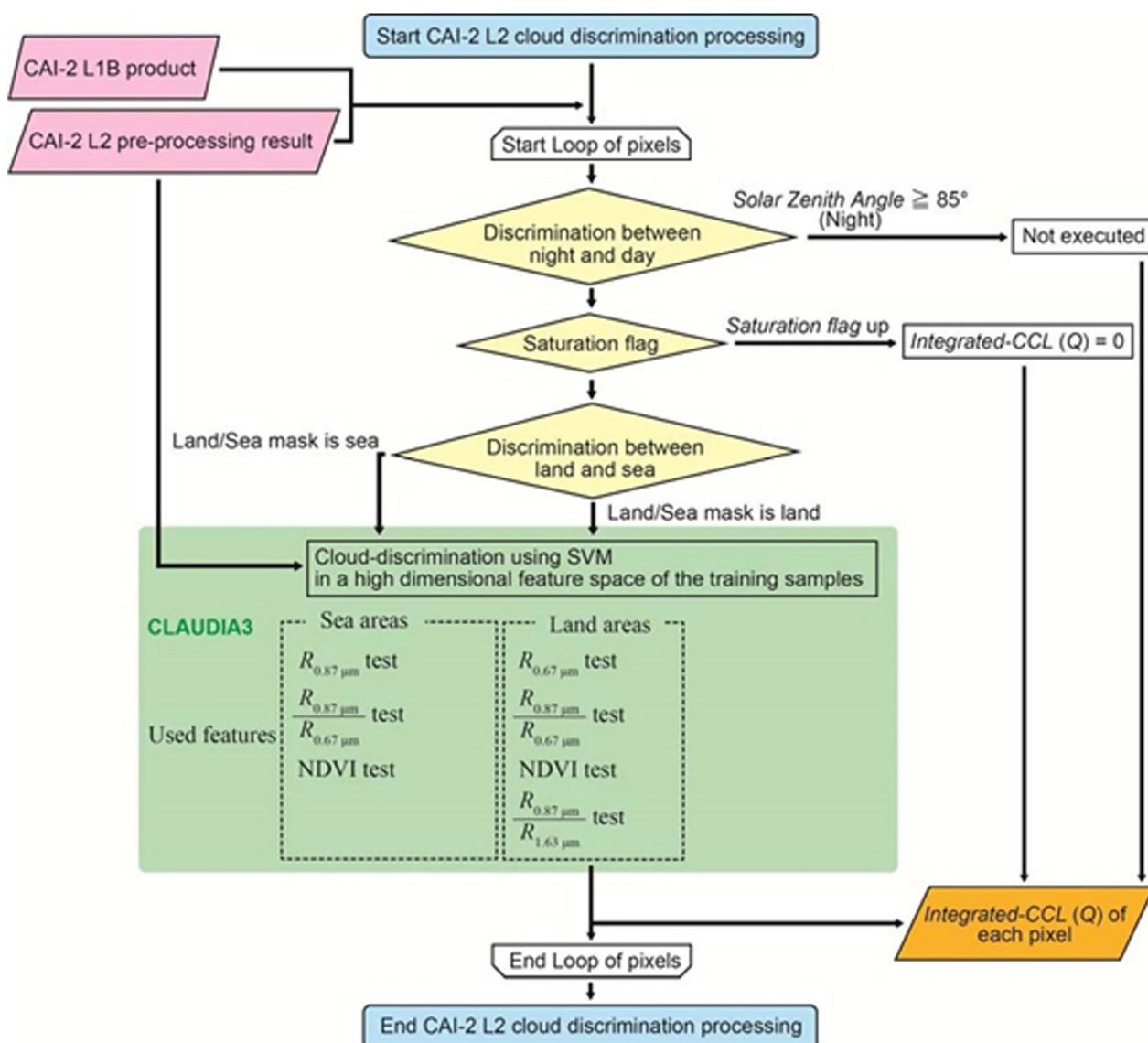


Fig. 16 Flowchart for CLAUDIA3-CAI, where CCL denotes the clear-sky confidence level, $R_{\text{wavelength}}$ signifies reflectance, and NDVI is the normalized difference vegetation index

aerosol absorption is expected to be enhanced. Particle size information can also be estimated using data of the visible-near-infrared band.

The TANSO-CAI-2 Level 2 aerosol products are intended to derive the aerosol optical thickness at a 1630 nm wavelength (AOT1630), which is necessary for improving the CO₂ derivation accuracy by TANSO-FTS-2. In addition, the retrieved aerosol products are the aerosol optical thickness at a 550 nm wavelength (AOT550) as an amount of the atmospheric aerosols, the aerosol Ångström exponent (AE) as particle size information, ePM_{2.5} as an equivalent amount of PM_{2.5} to elucidate the anthropogenic air pollutants, and the

black carbon volume fraction (BCF). The derived resolution of the product is 2 km×2 km in the Asian region, and 5 km×5 km otherwise (Fig. 18). Table 8 presents the TANSO-CAI-2 L2 aerosol property products and the required accuracy.

3.3.3 Aerosol retrieval algorithm

The multi-wavelength and multi-pixel method (MWPM) (Hashimoto and Nakajima 2017) is applied as the algorithm to retrieve TANSO-CAI-2 Level 2 aerosol products. The MWPM was developed for accurate derivation of aerosol characteristics, even in areas with inhomogeneous surface reflectance, such as urban areas for which it was difficult

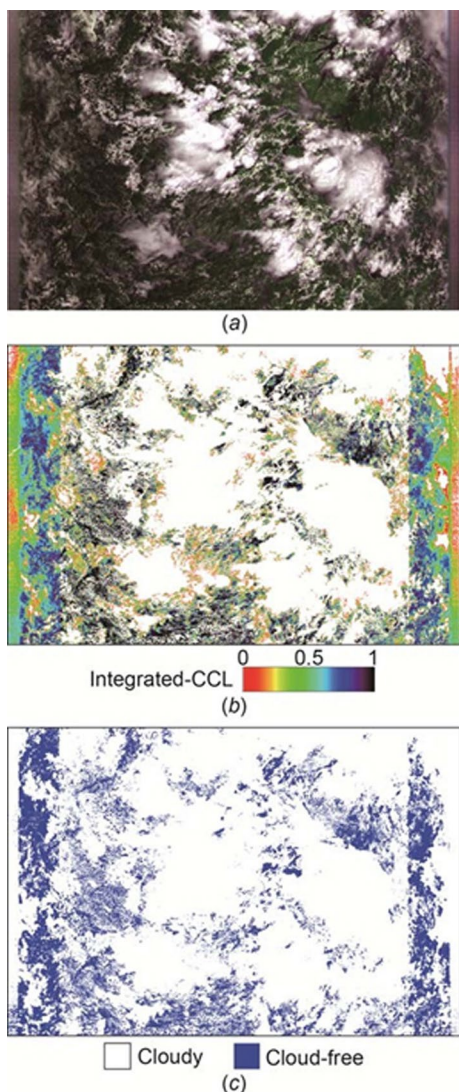


Fig. 17 Example of cloud discrimination result obtained using CLAUDIA3-CAI. **a** CAI L1B image (R, Band 2; G, Band 3; B, Band 1). **b** Output image from CLAUDIA3-CAI. **c** Result for an integrated-CCL threshold of 0.5

to derive aerosol characteristics from satellite images. This method expands the principle of the Kaufman Neutral method (Kaufman 1987) and simultaneously retrieves aerosol optical thickness and light absorption characteristics. It does so by simultaneously analyzing the observation points in the region where reflectance in the spatial direction changes.

The MWPM uses a combination of surfaces with different reflectance on the assumption of an aerosol that is distributed smoothly over the surfaces, as depicted in Fig. 19. Equation 10 expresses the apparent reflectance (R) by a single scattering approximation on a Lambertian ground surface as shown below.

$$R = A_g + [\pi m m_0 \omega P(\Theta) - (m + m_0) A_g (1 - \omega \gamma^+) + m_0 \omega \gamma^- A_g^2] \tau + O(\tau^2) \tag{10}$$

Therein, A_g stands for the surface reflectance; m and m_0 , respectively, represent inverses of the cosines of incident and scattered zenith angles. τ , ω , and $P(\Theta)$, respectively, denote the AOT, single scattering albedo (SSA), and phase function of the atmospheric air mass at scattering angle Θ . Also, γ^+ and γ^- , respectively, represent the downward and upward fractions of light scattering. The neutral reflectance (R_c) is a case in which $R_c = R = A_g$ in Eq. 10 corresponding to the middle case of Fig. 19 when a path radiance (first term on the right-hand side, RHS) and surface-reflected radiance (second term of the RHS) are canceled out, irrespective of the value of τ . For low-reflectance and high-reflectance surfaces, aerosols in the atmosphere, respectively, increase and decrease the apparent reflectance at the top of the atmosphere (TOA) with R_c as a boundary, depending on the light absorption characteristics of the aerosol particles. Presuming that AOT and other aerosol properties in the atmosphere do not change considerably in the horizontal direction, an optimal set of aerosol parameters (e.g., AOT, SSA, A_g) is found. Therefore, AOT and SSA are obtained by solving a set of radiative transfer equations (RTEs) using the spatial differences of surface reflectance (Hashimoto and Nakajima 2017).

The optimal method and smoothing constraint for atmospheric parameters are combined to solve the inverse problems for aerosol properties. Bayes' theorem is applied as an optimal method of problem solving to maximize the posterior probability density function $P(u|R)$ as shown below.

$$P(u|R) = \frac{P(R|u)P(u)}{P(R)} \tag{11}$$

Therein, $P(u)$ is a probability density function of event u . Also, $P(u|R)$ is a conditional probability density function where event u occurs under event R . Then, the smoothing constraint for atmospheric aerosol properties (i.e., a condition of minimizing the square of the second derivative of the aerosol spatial distribution with smoothing coefficients) is added to the optimal method.

$$\begin{aligned} \phi = & [R - f(u)]^T S_e^{-1} [R - f(u)] + (u - u_a)^T S_a^{-1} (u - u_a) \\ & + \sum_{ix} \gamma_{ix} (\mathbf{u}_{b,ix} + \mathbf{D}_{ix} \mathbf{u})^T (\mathbf{u}_{b,ix} + \mathbf{D}_{ix} \mathbf{u}) \\ & + \sum_{ix} \gamma_{ix} (\mathbf{u}_{b,ix} + \mathbf{D}_{ix} \mathbf{u})^T (\mathbf{u}_{b,ix} + \mathbf{D}_{ix} \mathbf{u}) \end{aligned} \tag{12}$$

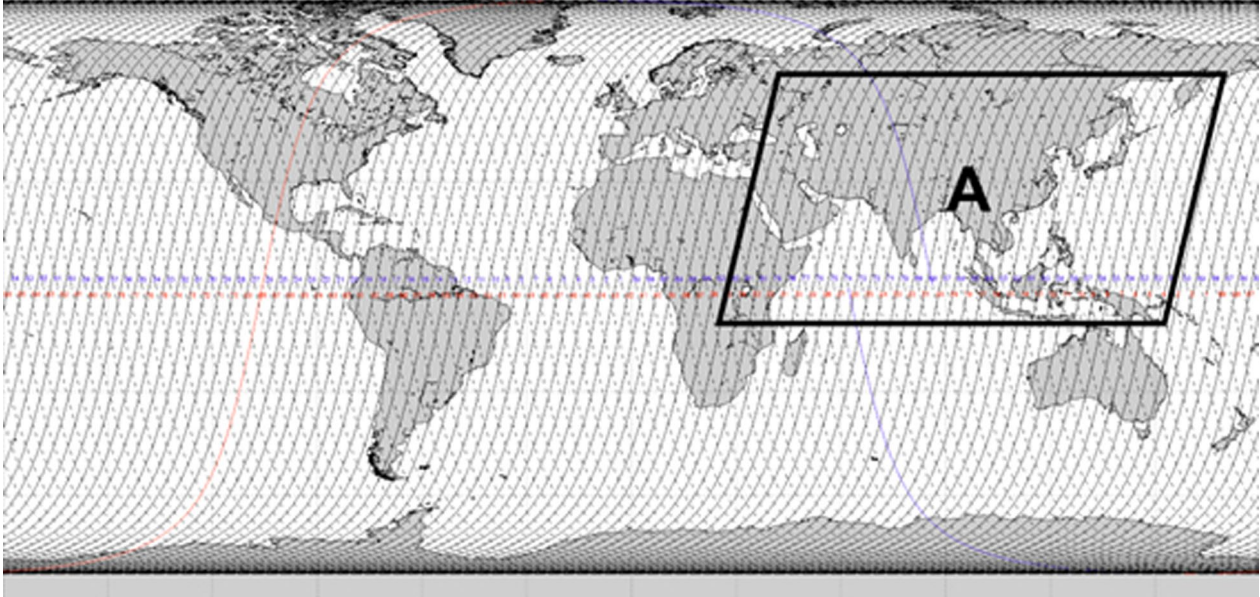


Fig. 18 Image of CAI-2 aerosol product with resolution of 2 km×2 km for the Asian region corresponding to GOSAT-2 passes 4–35 and frames 13–20, and 5 km×5 km for other areas

Table 8 GOSAT-2 CAI-2 L2 aerosol products

Product name	Accuracy	Unit	Resolution
AOT550	0.1	–	2 km×2 km & 5 km×5 km
AOT1600	0.1	–	
AE	0.3	–	
BCF	0.1	–	
ePM2.5	20	µg/m ³	

$$\frac{1}{\gamma} = S_x = \frac{1}{\Delta x} \int_x^{x+\Delta x} \left(\frac{\partial^2 u}{\partial x^2} \right)^2 dx, \quad (13)$$

$$\mathbf{R}_{ij} = [\ln R_{\text{band}1} \ln R_{\text{band}2} \cdots \ln R_{\text{band}10}]_{ij}^T, \quad (14)$$

$$\mathbf{u}_{ij} = [\ln \tau_{\text{fine}} \ln \tau_{\text{seasalt}} \ln \tau_{\text{coarse}} \ln f_{\text{BC}} \ln A_{g,\text{band}1} \ln A_{g,\text{band}2} \cdots \ln A_{g,\text{band}10}]_{ij}^T, \quad (15)$$

$$\mathbf{u}_{a,ij} = [\ln \tau_{a,\text{fine}} \ln \tau_{a,\text{seasalt}} \ln \tau_{a,\text{coarse}} \ln f_{\text{BC}a} \ln A_{ga,\text{band}1} \ln A_{ga,\text{band}2} \cdots \ln A_{ga,\text{band}10}]_{ij}^T, \quad (16)$$

In those equations, γ denotes the smoothing factor, x stands for a certain pixel, and Δx is the distance between two adjacent pixels to calculate the parameter’s smoothness. Also, \mathbf{R} is the measurement vector (i.e., observed apparent reflectance) at each measurement band. In addition, \mathbf{u} and \mathbf{u}_a , respectively, stand

for the state and a priori vectors. Actually, τ_{fine} , τ_{seasalt} , and τ_{coarse} , respectively, denote fine, sea, and coarse mode of aerosol optical thickness at 550 nm wavelength: AOT550fine, AOT550sea, and AOT550coarse. Total AOT550 is the sum of these AOT550s. f_{BC} is the volume fraction of black carbon (BCF). $A_{g,\text{band}N}$ is the surface albedo at band N . Subscript “a” represents the a priori value. Over the ocean, the wind speed at 10 m above sea level is used instead of the surface albedo. Five bands of forward or backward viewing are used, respectively, for analysis to avoid the sun glint region. \mathbf{S}_e and \mathbf{S}_a represent the covariance matrices of measurement errors and a priori values. \mathbf{B} is the boundary condition for the state vector. $\mathbf{f}(\mathbf{u})$ denotes a forward model (i.e., radiative transfer model). The forward model incorporates the radiative transfer model, accelerated

RSTAR using a neural network method (Takenaka et al. 2011). Developed at the University of Tokyo, RSTAR (Nakajima and Tanaka 1986, 1988; Sekiguchi and Nakajima 2008) can simulate radiation fields in the atmosphere–land–ocean system. Both AOT550 and BCF are derived by solving Eq. (12).

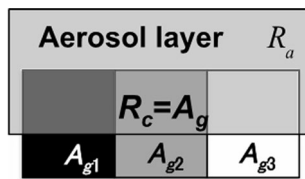


Fig. 19 Schematic illustration of the multi-wavelength and multi-pixel (MWMP) method. Satellite-received radiances for the smoothly distributed aerosol layer above Earth's surface of various reflectance (Hashimoto and Nakajima 2017)

For analyses, the region to be analyzed is divided into several small regions designated as subdomains (e.g., 5×5 pixels). Aerosol properties at each pixel in the subdomains are solved sequentially with a boundary condition.

3.3.4 Aerosol retrieval procedure

Figure 20 portrays the procedure for deriving TANSO-CAI-2 aerosol characteristics. First, using the observed data for one month before and after the product retrieval date (accounting for a total of 11 days), the surface reflectance is derived by the minimum and second minimum method (Fukuda et al. 2013). Then, using the surface reflectance and meteorological field data, aerosol properties such as total AOT550 and AOT1600 and BCF are retrieved by the MWPM. The AOT at each wavelength including 1600 nm is also derived from the retrieved AOT550s and the assumed aerosol model. Then, the Ångström exponent (AE) and ePM2.5 are calculated using the retrieved AOTs and BCF.

Using the wavelength characteristics of retrieved AOT at wavelengths of 441, 546, 672, and 865 nm, AE is calculated as

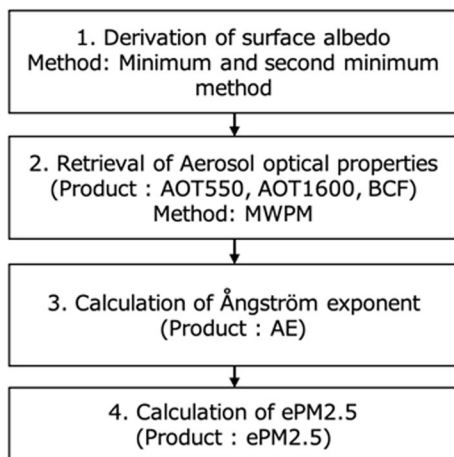


Fig. 20 CAI-2 aerosol property product derivation flow

$$\alpha = - \frac{n \sum_{i=1}^n \ln(\lambda_i) \ln(\tau_i) - \sum_{i=1}^n \ln(\lambda_i) \sum_{i=1}^n \ln(\tau_i)}{n \sum_{i=1}^n \{\ln(\lambda_i)\}^2 - \{\sum_{i=1}^n \ln(\lambda_i)\}^2}, \tag{17}$$

where α is the Ångström exponent, τ_i stands for the total amount of AOT at wavelength i , λ expresses the wavelength, and n represents the number of wavelengths used to calculate AE.

ePM2.5 is derived from the retrieved BCF, fine mode of AOT550, and the assumed aerosol particle size as

$$ePM2.5 = \frac{1}{m} \{ (1 - f_{BC}) \rho_{\text{sulfate}} + f_{BC} \rho_{BC} \} \int_{r_{\text{min}}}^{r_{\text{max}}} \frac{dv_{\text{fine}}}{d \ln r} d \ln r. \tag{18}$$

Therein, m is the aerosol height information parameter at unit meter. Also, ρ_{sulfate} and ρ_{BC} , respectively, denote the sulfate and black carbon particle densities. In addition, r stands for the particle radius; $dv_{\text{fine}}/d \ln r$ represents the volume size distribution of aerosol particles in fine mode.

4 Calibration and validation

4.1 Calibration

4.1.1 Overview

Sensor calibration is performed by pre-flight test (PFT) before the launch, and again on-board, with vicarious calibrations after launching. The TANSO-FTS-2 SWIR band and TANSO-CAI-2 observe sunlight reflected from the Earth's surface. The PFT is performed to evaluate the sensor output to radiance by the integrating sphere light source, which is calibrated using a standard radiometer. Consequently, the observation outputs can be converted into radiance by application of the radiometric conversion factors determined by the PFT results. Observation radiance of the TANSO-FTS-2 TIR band is achieved by conversion from the sensor output calibrated with deep space as a cold target and the onboard blackbody as a hot target on orbit. In the PFT, it is necessary to obtain a nonlinear response of detectors and polarization characteristics of the optics, which is difficult to determine on orbit.

4.1.2 Onboard calibration

The onboard calibration plan for TANSO-FTS-2 is presented in Table 9. Integrating sphere lasers are carried to confirm the instrument line shape (ILS) of Band 1 and Band 2. Thereby, the temporal stability on orbit can be tracked because of the PFT. Double-sided diffusers for solar irradiance calibration are operated to evaluate the degradation of the radiometric response of the SWIR band by observing both sides alternately. Lunar calibration for radiometric calibration for the SWIR band is planned for observation at the phase angle of +7° waning

Table 9 Onboard calibration for FTS-2

Onboard calibration	SWIR			TIR		Purpose, frequency
	B1	B2	B3	B4	B5	
ILS laser sphere	X	X				ILS stability because the PFT (once per 6 days)
Solar diffusers (both sides)	X	X	X			Radiometric response degradation (one side per orbit, the other side per 3 months)
Lunar calibration (Park to target)	X	X	X			Radiometric response degradation (per month, +7° waning near Full Moon)
Deep space				X	X	TIR onboard radiometric calibration (2 times in dayside, four times in nightside orbit)
Blackbody				X	X	TIR onboard radiometric calibration (2 times in dayside, four times in nightside orbit)
Phase transition cell				X	X	Blackbody thermometer verification (if necessary)
FOV camera						FOV confirmation (2 times per sounding in dayside orbit)

Table 10 Onboard calibration for CAI-2

Onboard calibration	Forward-looking (+20°)	Backward-looking (−20°)	Purpose, frequency
	B1–B5	B6–B10	
Lunar calibration (AT scan)	X	X	Radiometric response degradation (per month, +7° waning near full moon)
Lunar calibration (CT scan)	X	X	Pixel-to-pixel response correction (per 2 months, -7° waxing near full moon)
Nighttime calibration	X	X	Dark-time output (once per month, night ocean near new moon)

near a Full Moon. The appearance of the Moon is half the size of the TANSO-FTS-2 field of view (FOV). Radiometric calibration of the TIR band is performed on orbit by deep space and onboard blackbody two times dayside and four times nightside. The phase transit cell is carried to confirm the performance of the thermometer attached to the onboard blackbody. The FOV camera is operated to take photographs before and after intelligent pointing for the detection of cloud information of each sounding.

The onboard calibration plan for the CAI-2 is shown in Table 10. The TANSO-CAI-2 onboard calibration is operated by lunar calibration and nighttime calibration; it is not equipped with onboard calibrator. The lunar calibration for radiometry is planned to observe at phase angle of +7° waning near Full Moon

by along-track (AT) scanning with center pixels. The GOSAT-2 satellite is targeted to the Moon at a pitch angle of +20° for forward-looking bands, and at −20° for backward-looking bands. The lunar calibration for pixel-to-pixel response correction is operated by cross-track (CT) scanning with all pixels at a phase angle of −7° waxing near the Full Moon. Nighttime calibration for dark-time output is planned to observe the dark night ocean near a New Moon.

4.1.3 Vicarious calibration

Vicarious calibration after the launch is shown in Table 11 for the TANSO-FTS-2, and in Table 12 for the TANSO-CAI-2. A field campaign is conducted in summer at Railroad Valley (RRV) Playa, Nevada, USA,

Table 11 Vicarious calibration for FTS-2

Vicarious calibration	SWIR			TIR		Purpose, frequency
	B1	B2	B3	B4	B5	
RRV field campaign	X	X	X			Radiometric calibration (once per year, near summer solstice)
Inter-satellite comparison	X	X	X	X	X	Radiometric comparison with, GOSAT/FTS (1–2 days in 6-day revisit)
	X	X	X			OCO-2, TROPOMI
CEOS site monitor	X	X	X	X	X	AIRS, IASI, CrIS
						Radiometric monitor in several desert sites of CEOS recommendation (every 6 days)
Geometry						FOV camera geolocation compared with reference image

Table 12 Vicarious calibration for CAI-2

Vicarious calibration	Forward-looking B1–B5	Backward-looking B6–B10	Purpose, frequency
RRV field campaign	All bands	All bands	Radiometric calibration (once per year, near summer solstice)
Cross-calibration method	B2–B5 B1	B7–B10 B6	Radiometric calibration using, AERONET OC, VIIRS land desert radiance MOBY nLw data
Inter-satellite comparison	B2–B5 B1	B7–B10 B6	Radiometric comparison with, VIIRS OMPS OMI
CEOS site monitor	All bands	All bands	Radiometric monitor in several desert sites of CEOS recommendation (every 6 days)
Geometry	B4 B1–B3, B5 relative to B4	B9 B6–B8, B10 relative to B9	Absolute geolocation as a standard band compared with reference image Band-to-band registration relative to the standard band

by measuring the surface reflectance coincident with GOSAT-2 target observation for vicarious radiometric calibration of the TANSO-FTS-2 SWIR band and TANSO-CAI-2. The RRV experiment is a collaboration with NASA OCO-2/-3 team and other greenhouse gas projects. Cross-calibration for the TANSO-CAI-2 VNIR band is evaluated at the dark ocean target using AERONET Ocean Color (OC), and at a bright land desert target using VIIRS observed radiance. Those for UV bands 1 and 6 are evaluated using Marine Optical BuoY (MOBY) water leaving radiance (nLw). Inter-satellite comparisons with data from similar sensors, especially those of GOSAT, are planned that the TANSO-FTS-2 targets at some GOSAT TANSO-FTS observation points during 1 or 2 days in the GOSAT-2 6-day revisit, both at close orbits. The TANSO-FTS-2 SWIR band is compared with OCO-2 and TROPOMI, and the TIR band with AIRS, IASI and CrIS using simultaneous observation data. The TANSO-CAI-2 VNIR band is compared with VIIRS, whereas the UV band is compared with OMPS for Band 1, and with OMI for Band 6. The temporal stability of the radiometric response is also evaluated by monitoring desert sites recommended by Committee on Earth Observation Satellites (CEOS).

Geolocation is evaluated by comparison with a reference image after launching. The TANSO-FTS-2 geolocation is evaluated using a FOV camera image. The TANSO-CAI-2 geolocation is evaluated as a standard in Band 4 for forward-looking bands, and in Band 9 for backward-looking bands. Other bands are evaluated as band-to-band registration relative to the standard band.

4.2 Validation

4.2.1 Purpose and outline of validation

The product data observed using satellite remote sensing techniques are necessary for evaluation with other independent observation data for their scientific and political uses. Level 2 and higher level products will be validated and compared, respectively, whereas level 1 products will be calibrated. For validation, the product is evaluated with other independent observation data with better precision and well-known bias. For comparison, the product is evaluated with other independent observation data with equivalent or less precise or model data. During calibration, a physical quantity such as radiance is evaluated with independent observation data having better precision. Well-known bias and characteristics of instruments are assessed using various measurement methods.

A procedure for validation is the following, for example, selection of the validation data, quality check and screening of validation and satellite data, colocation, summary statistics, correlation analysis, and bias correction. For selection of the validation data, similarity, precision, and bias of data should be considered. Similarity signifies a similar physical quantity such as the column-averaged dry mole fraction such as XCO₂ or a profile of the dry air mole fraction to satellite data. If each group of data differs in quantity for validation and satellite data, then satellite or validation data conversion should be made of into same physical units. During quality checking and validation of satellite data, anomalies caused by instruments, weather conditions, and some phenomena should be discriminated according to the purpose of the validation level, such as preliminary, routine, geophysical,

advanced, and special-purpose detection for gas emission using statistical techniques. After quality checking, they should be removed. For collocation, various methods are used, such as geographical (Inoue et al. 2013), T700 (Wunch et al. 2011a), model-based (Guerlet et al. 2013), and geostatistical (Nguyen et al. 2014). They are summarized in a report by Nguyen et al. (2014). Then, validation and satellite data are made summary statistics (mean and median with or without weight) with or without averaging kernel and prior corrections. Next, for correlation analysis, validation and satellite data are compared with or without weights. When weights for both data are considered for correlation analysis, the so-called York method is used. Characteristics such as bias and scatter are eventually estimated. If there are validation criteria for each product as a satellite mission and statistics achieve them, the products are recognized as validated. However, statistical examination using this procedure can be applied for validation. If possible, satellite data are recommended to be corrected against their biases using empirical linear regression. This motivation and various methods are summarized in a report by Inoue et al. (2016). Normally, correlation analyses between the satellite biases and simultaneously retrieved auxiliary parameters are made. These correlations are used to bias-correct the GOSAT data, thereby removing these spurious correlations.

4.2.2 Overview of the GOSAT-2 products validation plan

As validation sources for X_{CO_2} , X_{CH_4} , X_{CO} , and X_{H_2O} retrieved from the SWIR spectra onboard GOSAT-2 TANSO-FTS-2, TCCON is a primary validation source. TCCON is a worldwide network of ground-based FTSs that provide time series of column-averaged abundances of various atmospheric constituents. These constituents including CO_2 , CH_4 , N_2O , HF , CO , H_2O , and HDO are retrieved from near-infrared solar absorption spectra similar to GOSAT-2 using a nonlinear least-squares fitting algorithm known as GFIT (Wunch et al. 2010, 2011a, 2011b). The TCCON data are also useful for the validation of satellite vertical profiles of CO_2 and CH_4 after conversion into the same physical quantities. In addition to the TCCON data, the obtained Network for the Detection of Atmospheric Composition Change (NDACC) FTS data are useful. The Infrared Working Group (IRWG) represents a network of infrared Fourier-transform spectrometers that is part of NDACC. An overview of NDACC is described in a report by De Mazière et al. (2018): It is a multi-national collection of more than 20 high-resolution spectrometers that regularly record the atmospheric absorption spectrum from sites distributed from pole to pole. The absorption spectra are used to retrieve concentrations of a number of the gaseous

atmospheric constituents, including O_3 , HNO_3 , HCl , HF , CO , N_2O , CH_4 , HCN , C_2H_6 , and $ClONO_2$. Because the NDACC FTS data are column abundances and vertical profiles of constituents, they are useful to validate SWIR and TIR products of GOSAT-2. In addition to FTS data, DIAL (e.g., CO_2 , Sakaizawa et al. 2009; O_3 , Uchino et al. 2017), other portable solar light observation instruments such as portable FTS network called Collaborative Carbon Column Observing Network (COCCON) (Frey et al. 2019), Optical Spectrum Analyzer (OSA, Kobayashi et al. 2010; Kawasaki et al. 2012), fiber-etalon sun-photometer (Kobayashi et al. 2010; Kawasaki et al. 2012), and a laser heterodyne radiometer (Wilson et al. 2014) are used.

Profiles of CO_2 , CH_4 , H_2O , and other gases retrieved from the TIR spectra can be validated using aircraft data such as the Comprehensive Observation Network for TRace gases by AirLiner project (CONTRAIL) (Machida et al. 2008), In-service Aircraft for a Global Observing System (IAGOS) core (Filges et al. 2015), the NOAA Earth System Research Laboratory/Global Monitoring Division (ESRL/GMD) (Xiong et al. 2008; Sweeney et al. 2015), the US Department of Energy (DOE) (Biraud et al. 2013; Schmid et al. 2014), and CO_2 sonde (Ouchi et al. 2019), and AirCore (Karion et al. 2010). Their profiles can also be useful for validating the SWIR products by conversion into X_{gas} .

Surface measurements of greenhouse gases (e.g., WDCGG 2022) can also provide a useful comparison for SWIR and TIR products.

Satellite data of greenhouse gases are useful for comparison to GOSAT-2 products. SWIR data from GOSAT, OCO-2, TanSat, TROPOMI are contributed to compare GOSAT-2 SWIR products. TIR data from AIRS, IASI, MOPITT, etc., are useful to compare the GOSAT-2 TIR products.

Solar-induced fluorescence (SIF) provides reliable information of plant physiological functioning at a large spatial scale. Actually, SIF can be validated using ground-based (e.g., Julitta et al. 2016) and aircraft (e.g., Garzonio et al. 2017) SIF data recorded with a hyperspectral spectrometer. Moreover, SIF can be compared with satellite data provided by GOME-2, GOSAT, OCO-2, TanSat, FLEX, and others, in addition to vegetation model data.

In situ data and ground-based remote sensing data from AERONET and SKYNET (Nakajima et al. 2020a, 2020b) are used to validate $PM_{2.5}$ and black carbon (BC) from TANSO-CAI-2. Satellite data from MODIS, EarthCARE, and others can also be useful for comparison. As advanced validation to improve the GOSAT data quality further, investigation can be made about the effects of aerosols and thin cirrus clouds on the GOSAT-2 product over Rivulets, Tsukuba, Saga, Burgos, and Lauder using FTS, lidar, and skyradiometer.

Campaign observation is expected to be important where validation data are sparse. Under such circumstances, combinations of portable instruments and aircraft and satellite observation are recommended according to the campaign purposes.

4.2.3 Ongoing validation activities of the GOSAT-2 products

After starting the L2 processing, we have been conducting validation analysis using TCCON data for XCO₂, XCH₄, XCO, and XH₂O. We have made evaluations of the influences of aerosol and thin cirrus on them using data obtained from skyradiometer and lidar. We also have started intercomparisons of XCO₂, XCH₄, and XCO with OCO-2, TROPOMI, and model data. The CO₂ profile has been compared with those taken from CONTRAIL and model data. The SIF data have been compared with those from satellite data from OCO-2, etc. Moreover, the AOT data from TANSO-CAI-2 have been validated using the AERONET and SKYNET data; also, BC and PM_{2.5} have been compared with surface BC and PM_{2.5} data. Some of the validation analyses have been used for review processes in public release.

5 Scientific goals

5.1 Global inversion

At the moment, available estimates of surface fluxes of greenhouse gases (GHGs) still have marked degrees of uncertainty because our understanding of flux mechanisms remains insufficient. Many gaps exist in in situ observation networks. Satellites, including GOSAT-2, that observe atmospheric mole fractions of GHGs are expected to reduce those uncertainties because of their wide spatial coverages. Generally, an atmospheric transport model is used to connect surface fluxes with observed atmospheric mole fractions. Based on those findings, an inverse analysis is performed to estimate surface fluxes. An inverse analysis is useful in that it provides quantitative estimates of spatiotemporal variations of surface fluxes consistently with observed variations of atmospheric mole fractions. In a typical global inverse analysis, surface fluxes are estimated on a much larger scale (a few 100 km) than a footprint of satellite observations (a few to 10 km), because of the computationally demanding simulations of an atmospheric transport model. However, because satellite retrievals represent partially column-averaged mole fractions and because they consequently have large representativeness, satellite observations can be major input data of a global inverse analysis. Such a global inverse analysis is expected to provide valuable implications of large-scale (sometimes interhemispheric scale) spatial patterns and seasonal variations of surface GHG fluxes.

In the GOSAT-2 project, the Nonhydrostatic Icosahedral Atmospheric Model (NICAM)-based Transport Model (NICAM-TM) (Satoh et al. 2014; Niwa et al. 2011) is used to prepare prior estimates of retrieval calculations (i.e., the L2 product). Furthermore, the inverse analysis based on NICAM-TM, which is designated as NICAM-based Inverse Simulation for Monitoring (NISMON) CO₂ and CH₄, provides surface flux estimates of CO₂ and CH₄ using each L2 product of GOSAT-2 (i.e., the L4 products) (Saito et al. 2019). NISMON employs the 4D-Var method, by which forward and backward transport simulations are performed iteratively to optimize fluxes (Niwa et al. 2017a, 2017b). The optimizer is based on a quasi-Newtonian method with the Broyden–Fletcher–Goldfarb–Shanno (BFGS) algorithm (Fujii 2005). The L4 products of GOSAT-2 are derived from NISMON analyses with a horizontal resolution of ca. 223 km, which is the mean interval of the “glevel-5” NICAM grid (Fig. 21). It is noteworthy that the NICAM grid shapes are hexagons or pentagons, which are generated by dividing an icosahedron recursively (Satoh et al. 2014). The temporal resolution of optimized fluxes is set as monthly. As elaborated in Niwa et al. (2017b), surface fluxes are optimized with prescribed spatial correlations in the prior errors. In the experiment of reported by Niwa et al. (2017b) with ground-based observations, the error correlation scales are set as 500 km for terrestrial areas and as 1000 km for oceans. These error correlations act as a smoother and improve flux estimates. That would be true even for the case with satellite data. Therefore, although fluxes are optimized at each model



Fig. 21 Model grid of the “glevel-5” NICAM. The mean grid interval is ca. 223 km (Satoh et al. 2014)

grid, the practical resolution of the fluxes that the satellite data constrain would be several times as large as the model grid. This important point must be recognized before analyzing the L4 products.

Estimated surface fluxes by inversion have theoretical errors named “posterior errors,” which are derived from diagonal elements of the posterior error covariance matrix. Because that matrix size is $n \times n$, where n denotes the number of estimated fluxes (i.e., the number of model grids multiplied by the temporal resolution), it is not a trivial task to obtain posterior errors. However, NISMOM uses a state-of-the-art method developed by Niwa and Fujii (2020) to estimate posterior errors. By investigating the degree to which posterior errors are reduced from prior errors, one can evaluate the strengths of observational constraints, an example of which is presented in Fig. 22. Posterior errors in Fig. 22 are derived using the

same settings as those reported by Niwa et al. (2017b), but the ground-based observations are replaced by the GOSAT TANSO-FTS SWIR data for 2010. Because they depend strongly on the settings of prior errors and model-observation mismatch errors, which are key tuning parameters of an inversion, the values themselves in Fig. 22 might not be valid for a practical satellite inversion. Nevertheless, spatiotemporal patterns give valuable implications. As shown in Fig. 22, the satellite constraints are marginal in winter high-latitude areas. This is true because satellite retrievals are not available where sunlight does not exist. In addition, prior errors of terrestrial biosphere fluxes are often set as small because of the low biosphere activity in winter, resulting in weak observational constraints. In summer mid-latitudes to high latitudes and tropical areas, the satellite constraints are considerably strong. This fact is especially important for

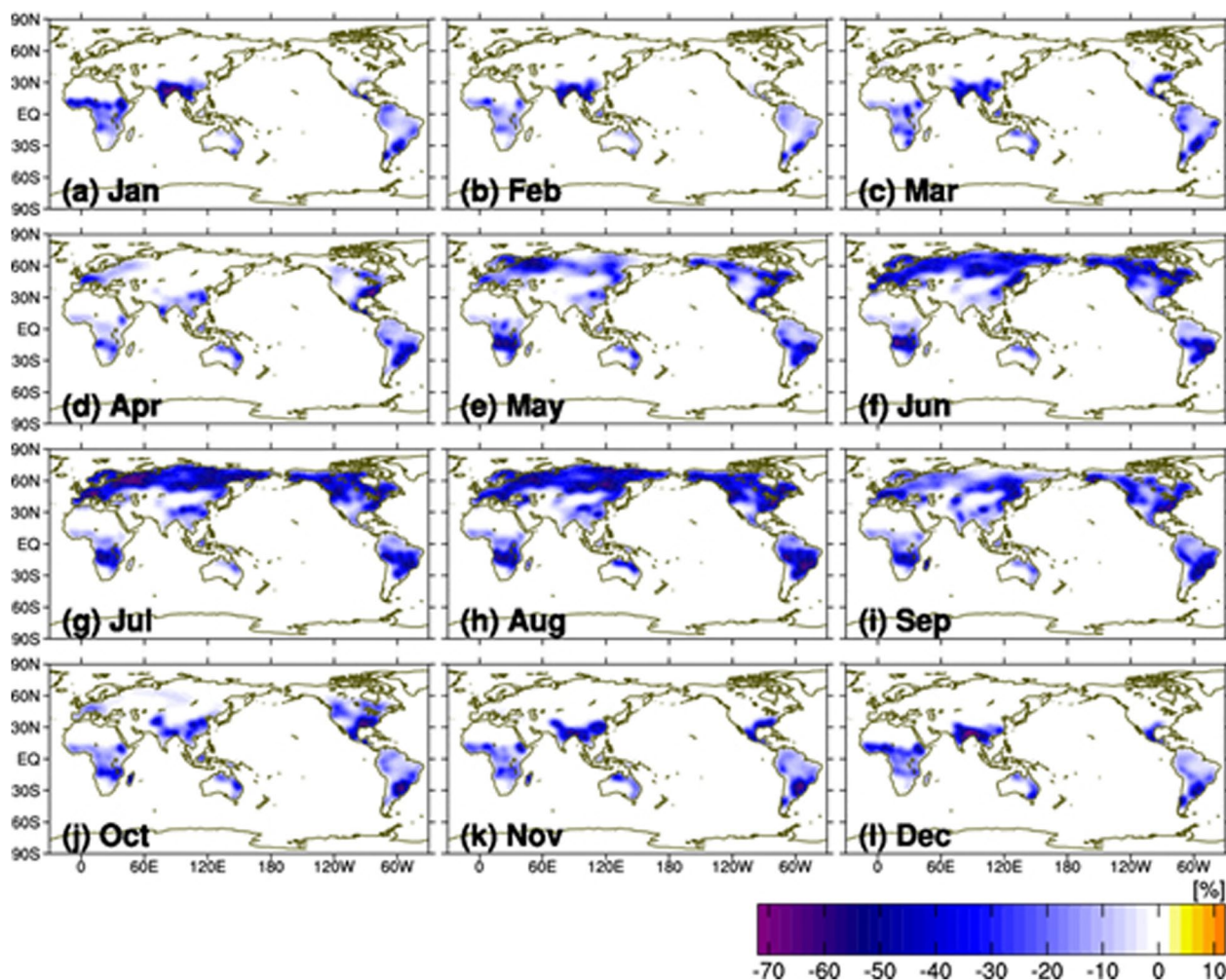


Fig. 22 Error reduction ratios of CO₂ flux estimates for each month. They are derived by the same settings of Niwa et al. (2017b), but with the GOSAT-1 SWIR data for 2010. The error reduction ratio is defined as $\frac{\sigma_{\text{pos}} - \sigma_{\text{pri}}}{\sigma_{\text{pri}}} \times 100$, where σ_{pos} and σ_{pri} , respectively, represent the posterior and prior errors. This represents observational constraints. Here, the observation model mismatch uncertainty is assumed as 2 ppm for individual SWIR data

Siberia and tropical areas, where ground-based observation networks are extremely sparse. This picture would be true also for GOSAT-2.

5.2 Regional targets

Monitoring CO₂ emissions from large-scale CO₂ emission sources such as electric power plants and urban areas with heavy traffic is an important task. To this end, we have conducted specific observations by GOSAT targeting urban areas and power plants, particularly, intensive observations of the Kanto Plain, including Tokyo started in 2010. Similarly, we are conducting target observations with GOSAT-2 over major megacities around the world. An example of the observed data is presented in Fig. 23. These observation data are combined with the ground-based observation data, after which they are used as input data to regional transport models. The CO₂ emission intensity was estimated using inverse analysis.

By improving the SNR and by reducing the radiance biases, the estimation accuracy of the boundary layer (mixed layer) altitude obtained from the vertical distribution analysis of the temperature using the TIR band is improved. Using this information, it is expected that the accuracy of the method used for estimating the CO₂ concentration near the surface layer will be improved

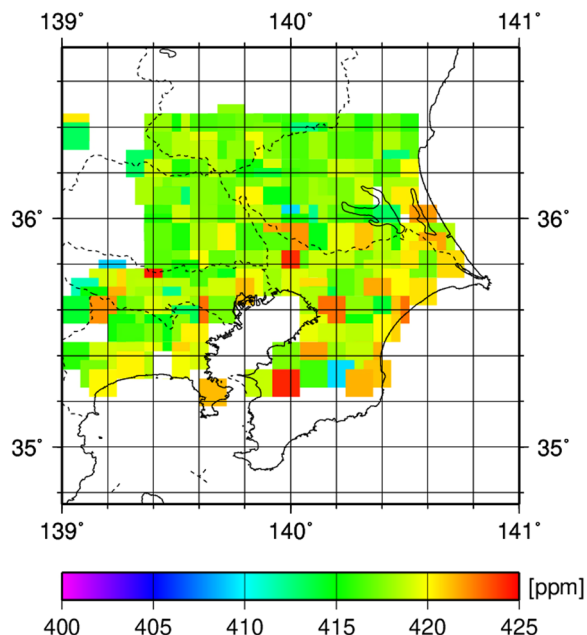


Fig. 23 Example of XCO₂ composite map observed by GOSAT-2 with its specific target observation conducted from 2019 to 2022. GOSAT-2 level 2 (Ver.01.07) data observed in winter season (November–February) are used

through the combined analysis of the columnar CO₂ concentration retrieved from SWIR band data and the upper air concentration obtained from the TIR band (Imasu 2019). This method is particularly effective for urban areas where surface temperatures are high. For such situations, the thermal contrast, which is defined by the difference between the atmosphere and the surface temperature, is high. For that reason, the resolution of the vertical distribution of air temperature in the lower atmosphere is expected to be improved.

Another major improvement of TANSO-FTS-2 is that the wavelength range of SWIR band 3 for carbon monoxide (CO) measurement has been expanded. Because CO is a substance of combustion origin, it is expected that information related to differences between CO₂ of combustion origin and CO₂ of vegetation respiratory origin in urban areas can be obtained (Takekawa et al. 2004).

Hotspots, in a climatological sense, are large carbon stores and large carbon sinks. These are areas that are susceptible to climate change and land use changes. They can be major future sources of greenhouse gas emissions. Pre-identifying and then monitoring these hotspots continuously will support early detection of signs of carbon cycle change attributable to climate change.

Specific areas include land areas where global warming effects are expected to be greater at high latitudes, especially areas where CO₂ absorption increases with extension of the growing season, areas where CO₂ absorption decreases because of dryness during summer, areas where CO₂ and CH₄ emissions increase because of large-scale forest fires, areas where albedo is expected to change because of early snowmelt, areas where frozen soil melts and the accompanying increase in CO₂ and CH₄ emissions from the soil occurs, and areas where CH₄ hydrates exist.

5.3 Solar-induced chlorophyll fluorescence (SIF)

Photosynthetic CO₂ assimilation by plant vegetation, known as gross primary production (GPP), is the largest carbon flux on the Earth surface; it is also an important driver of global climate (Global Carbon Project 2017). Its rate is extremely sensitive to environmental variation. For that reason, it varies spatiotemporally to a great degree. To date, many efforts have been undertaken using various techniques, including satellite remote sensing, to monitor the GPP of various forms of vegetation. Earlier satellite remote sensing studies have used reflectance spectral indices (e.g., normalized difference vegetation index, NDVI) that estimate plant status related to structural or pigment properties such as the leaf area index (White et al. 1997) and leaf chlorophyll content (Daughtry et al. 2000). Although these data are useful

to predict the potential GPP (Running et al. 2004), they are insufficient for assessment of physiological changes of the photosynthetic system that often occur without changes in leaf area or chlorophyll content. Therefore, such vegetation indices are insufficient to assess spatiotemporal variations in GPP. In recent years, complementing such reflectance-based indices, solar-induced chlorophyll fluorescence (SIF) has been used to estimate GPP and plant stress (e.g., Parazoo et al. 2013, 2014; Liu et al. 2017). Chlorophyll fluorescence is a radiation in the red and near-infrared regions with two peaks at approximately 690 and 740 nm emitted by chlorophyll-*a* molecules. A large part of the light energy absorbed by chlorophyll is used for photochemistry. Therefore, carbon assimilation and photorespiration, to the extent that it remains, are lost as heat and fluorescence (Baker 2008; Porcar-Castell et al. 2014). Chlorophyll fluorescence yield changes depending on the status of photochemistry and heat dissipation. In fact, it provides various information related to the photosynthetic machinery (Hikosaka and Tsujimoto 2021). However, detecting SIF in the field has been challenging (Meroni et al. 2009) because the magnitude of SIF is much lower than the reflected radiation from leaves. At a leaf scale, pulse amplitude-modulated (PAM) fluorimeters have been able to detect chlorophyll fluorescence. They have been used in many physiological and ecological studies. In remote sensing, including satellite observations, SIF can be retrieved using high-spectral resolution measurements using the Fraunhofer depth method (Meroni et al. 2009).

The first SIF retrieval from satellite observations on a global scale was conducted with TANSO-FTS onboard GOSAT (Frankenberg et al. 2011c, 2012; Joiner et al. 2011; Guanter et al. 2012). Band 1 of TANSO-FTS covers the overlapping part of SIF and Fraunhofer lines in the near-infrared region with high spectral resolution. Subsequently, SIF has been retrieved from the data measured by satellites aiming at measuring GHGs concentration, such as SCIAMACHY onboard ENVISAT (Joiner et al. 2012), GOME-2 of Op-A and B (Joiner et al. 2013), OCO-2 (Sun et al. 2017), TROPOMI of Sentinel 5P (Guanter et al. 2015; Köehler et al. 2018), and TanSat (Du et al. 2018). These satellite SIF data have been used for mutual validation (e.g., Oshio et al. 2019).

TANSO-FTS-2 onboard GOSAT-2 is also available to retrieve SIF. Those SIF data are provided as one standard product. GOSAT-2 is expected to provide SIF data that have higher validity than those of GOSAT because of the intelligent pointing system. Generally speaking, satellites are unable to observe SIF accurately in cloud-covered areas. The intelligent pointing system is expected to increase the number of clear-sky observations and to enhance our understanding of climate change effects on terrestrial ecosystems, especially in tropical rainforests, which are often cloud-covered.

Figure 24 portrays a global map of GOSAT-2 SIF of August 2019. Actually, SIF was greatest in areas with tropical vegetation such as the Amazon, Central Africa, and Southeast Asia, which are known to have the highest GPP on Earth. By contrast, it was lowest in desert areas

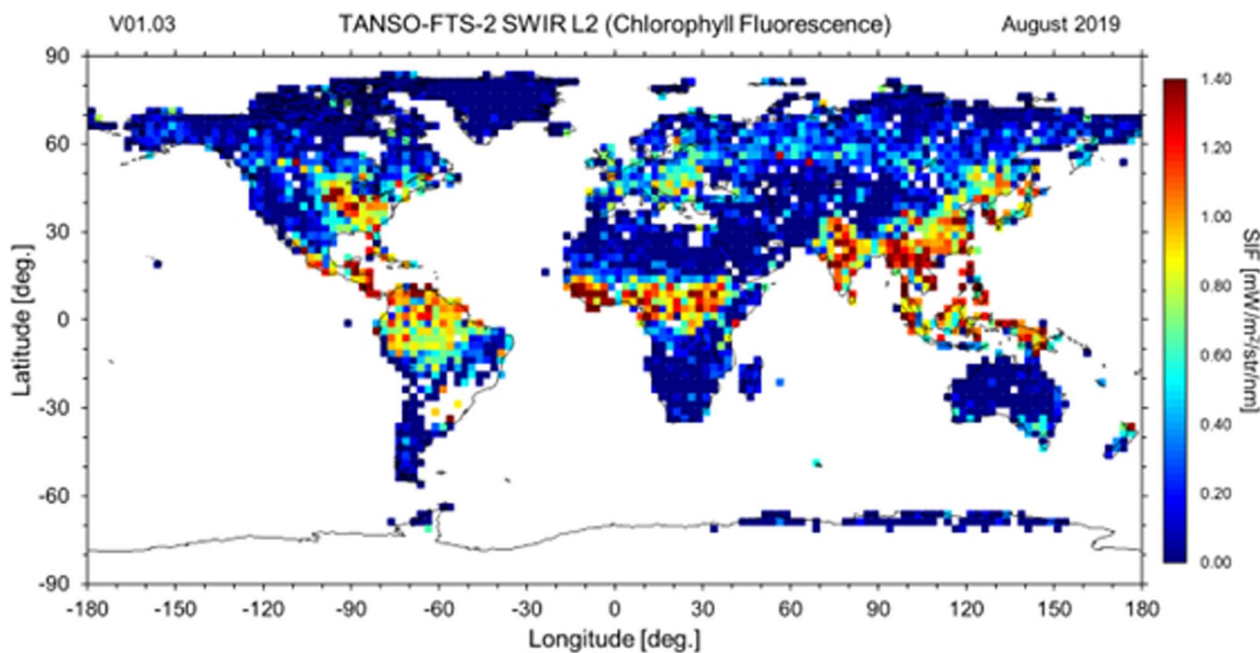


Fig. 24 Global map of GOSAT-2 SIF (TANSO-FTS-2 SWIR L2 product, V) in August 2019. Monthly averages of SIF in 2×2 degrees grid are shown

such as the Sahara and Arabia, and the Arctic and Antarctic regions, where vegetation is scarce. Results demonstrated that SIF is correlated linearly with data-driven GPP estimates at global and/or annual scales (Frankenberg et al. 2011c; Guanter et al. 2012; Sun et al. 2017). The correlations are rationalized to the light use efficiency (LUE) model for GPP by Monteith (1972). Actually, GPP is regarded as the product of proportional to incoming photosynthetically active radiation (PAR), the fraction absorbed PAR (fAPAR) by vegetation, and the LUE for GPP. Similarly, SIF is conceptualized as the product of PAR, fAPAR, LUE for SIF. These equations can be combined as simple correlations between GPP and SIF (Lee et al. 2013; Guanter et al. 2014; Sun et al. 2017). This approach has been used for various ecosystems such as those of the Amazon rainforest (Parazoo et al. 2013) and the boreal forests of Eurasia and North America (Walther et al. 2016). However, the relation between GPP and SIF differs depending on the season (Thum et al. 2017), vegetation type, and canopy structure (Guanter et al. 2014; Migliavacca et al. 2017). Another approach is using the radiative transfer models, which simulate underlying mechanisms such as the biophysiological processes and scattering and reabsorption effects on SIF signals within a canopy. The SCOPE model, developed by van der Tol et al. (2009), is a 1-D radiative transfer, photosynthesis, and energy balance model. SCOPE has contributed to assessment of GPP from SIF (Lee et al. 2013; Zhang et al. 2014; Thum et al. 2017).

Using the SCOPE-like model and carbon-cycle models, GOSAT-2's SIF would enable us to improve the accuracy of the L4 product of GOSAT-2, CO₂ flux. Accurate estimation of GPP helps elucidate the consequences between meteorological conditions and CO₂ assimilation functions of vegetation, and to predict future trends. Additionally, used in conjunction with XCO₂ data, it might contribute to estimation of anthropogenic CO₂ emissions.

5.4 Air pollution monitoring and related climate studies

One main objective of the GOSAT-2 satellite mission is air pollution monitoring. As reported by the World Health Organization (WHO 2016) and the Organization for Economic Co-operation and Development (OECD 2020), global health effects of air pollution are as great as annual excess mortality of 3–4 million people. Furthermore, the IPCC Special Report on Global Warming of 1.5° and the Sixth Assessment Report (AR6) assessment report have concluded that marked reduction of the Short-Lived Climate Forcer (SLCF) along with CO₂ reduction is necessary to attain the 1.5° reduction target

for global warming mitigation (IPCC 2018, 2021). Recent studies indicate that a SLCF reduction scenario must be designed carefully by the full analysis of complex negative and positive feedback processes among the constituents (Stohl et al. 2015; Nakajima et al. 2020a, 2020b). A small but significant surface temperature decrease by the total BC reduction, for example, is explained by counterwarming effects of increases in the upper clouds because of atmospheric stability change (Takemura and Suzuki 2019).

Earth observation by the GOSAT-2 satellite contributes to air pollution monitoring and to collecting useful knowledge for the SLCF climate impacts with their unique simultaneous measurements of CH₄, CO, and aerosols with the TANSO-FTS2 sensor with a 9.7 km FOV and the TANSO-CAI-2 imager with two UV bands of 340 nm and 380 nm and with a 500 m FOV. The fine FOV of TANSO-CAI-2 is especially useful for pollution monitoring over heterogeneous land surfaces such as city areas and coastal zones when data are analyzed using the MWMP algorithm (Hashimoto and Nakajima 2017; Shi and Nakajima 2018; Shi et al. 2019). Figure 25 shows that the two UV bands can detect smoke aerosols clearly in the case of an Australian forest fire (JAXA 2020; Nakajima et al. 2021). Estimation of the BC fraction is promising, as reported by Shi et al. (2020) for the Australian forest fire case, and for the Indian case (Gogoi et al. 2021, 2022).

Recent reports of close correlation of CO₂ concentration with short-lived atmospheric materials, i.e., NO₂ and aerosols, in model simulations and airborne and satellite observations around large-scale emission sources (e.g., Goldberg et al. 2019; Fujinawa et al. 2021) indicate that the combination of GOSAT-series satellites with other satellites for short-lived material observation is a promising method for providing wide-area information that is useful for emission inventory construction and the United Nations Framework Convention on Climate Change (UNFCCC) global stock taking routine. Itahashi et al. (2019) demonstrated an update of REAS NO_x inventory through assimilation of OMI-observed NO₂ data with short turn-around time of less than several years. This benefit is expected to be increased in the next-phase global monitoring system by Geostationary Environment Monitoring Spectrometer (GEMS), Tropospheric Emissions: Monitoring Pollution (TEMPO), and Sentinel-4 geostationary satellites (Kim et al. 2020). Therefore, designing a satellite that is able to monitor NO_x and GHGs simultaneously is expected to be important for future work.

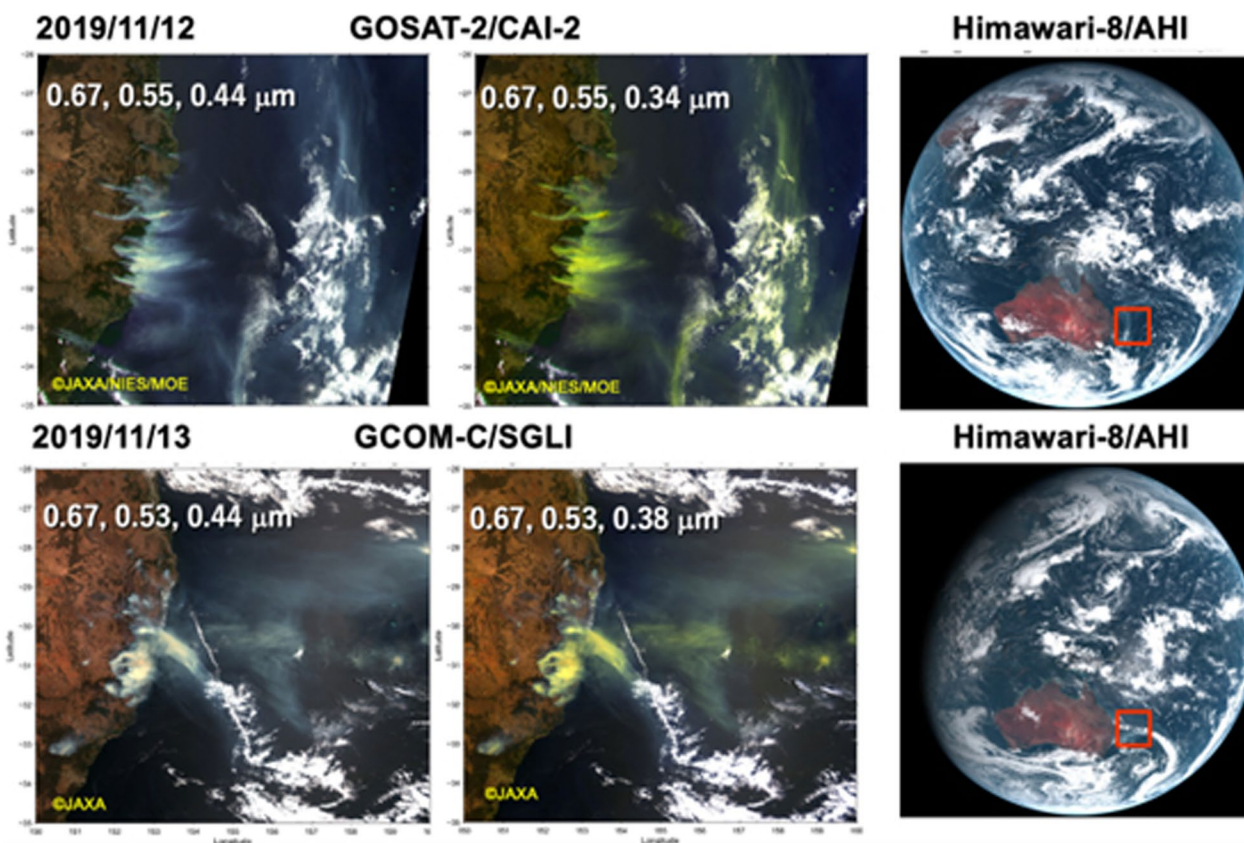


Fig. 25 Aerosol observation of the Australian forest fire smoke of November 12–13, 2019, by Himawari-8, GCOM-C/SGLI, and GOSAT-2/CAI-2. Results show that the introduction of two ultraviolet bands is useful to distinguish smoke from clouds. Cited from JAXA (2020) and Nakajima (2021)

6 Conclusions

Compared to the first GOSAT sensors, the GOSAT-2 equipped sensors have demonstrated improved performance in most respects. The quality and quantity of observation data are expected to be improved accordingly. The signal-to-noise ratio (SNR) is improved in both the SWIR and TIR bands of TANSO-FTS-2, which is the main sensor of GOSAT-2. This improvement will ultimately enhance the accuracy of greenhouse gas concentration analysis. In addition, because of the improved SNR in the SWIR band, the northern limit at which data are obtainable in high-latitude regions of the Northern Hemisphere in winter, where observation data were heretofore unavailable because of weak signal strength, has moved to higher latitudes. As more and better data are obtained, progress in carbon cycle research for high-latitude regions is anticipated. Moreover, it is estimated that the improvement of the SNR in the TIR band can be considerable. Particularly, the resolution of the vertical concentration distribution of CO₂ and CH₄ has been improved drastically. Using the CO₂ column concentration obtained from the SWIR band and the upper air concentration of CO₂ obtained from the TIR band in

combination, the retrieved CO₂ concentrations near the ground surface, which are important for estimating the amount of CO₂ emission and uptake, are obtainable. This benefit of GOSAT/GOSAT-2 is not provided by satellites equipped with other similar sensors.

The first function introduced into GOSAT-2 which has not been implemented in GOSAT is an intelligent pointing mechanism: a cloud area avoidance function using the in-field camera of TANSO-FTS-2. This function can be expected to increase the amounts of observation data globally and to improve the estimation accuracy of CO₂ emissions and uptake intensity. The effect is expected to be strong, especially in the tropics, because the most common cloud type is cumulus there. The intelligent pointing system can avoid clouds effectively.

Another major change of TANSO-FTS-2 is that the wavelength range of Band 3 of SWIR has been expanded for measuring carbon monoxide (CO). Because CO is a substance originating from combustion, it is used to evaluate the effects of human activities in urban areas and biomass burning in the field. Particularly, black carbon-type aerosols can be measured by TANSO-CAI-2 for biomass burning as well as CO₂ and CO by TANSO-FTS-2.

The partitioning ratio of these three substances might provide information that characterizes the fire, such as combustion completeness. In fact, GOSAT-2 is the only satellite that can simultaneously measure Short-Lived Climate Forces (SLCF) such as CH₄, BC, and ground-level ozone together with CO₂.

The ultimate goal of most greenhouse gas observation satellite projects, including GOSAT and GOSAT-2, is elucidation of anthropogenic greenhouse gas emissions and their effects on the carbon cycle and climate. However, to extract only the effects of anthropogenic origin from the information obtained using these satellite-based sensors, it is necessary to evaluate and eliminate the effects of natural origin which are included therein. Eliminating these influences is mainly a question of how to achieve accurate evaluation of CO₂ emissions (respiration) and absorption (photosynthesis) by terrestrial ecosystems. One method is cooperation with satellites launched to evaluate the dynamics of terrestrial ecosystems. By combining related to various activities of terrestrial ecosystems such as the vegetation index and heat dissipation (photochemical reflection index) obtained from these satellites with SIF information obtained from GOSAT-2, the physiological and ecological activity of vegetation can be better evaluated. In this way, the combined use of various satellite data makes it possible to acquire more advanced information related to the carbon cycle.

Future research undertaken to elucidate the global carbon cycle including greenhouse gases and research to evaluate the global environment are expected to become more sophisticated and increasingly complicated. Therefore, achieving sufficient scientific results with only a single satellite project is difficult. The only solution is addressing these issues through collaboration with numerous satellite projects and extensive international cooperation.

Abbreviations

4D-Var	4-Dimensional variational method
ACTM	Atmospheric chemistry transport model
AE	Ångström exponent
AERONET	Aerosol RObotic NETwork
AIRS	Atmospheric InfraRed Sounder
AOT	Aerosol optical thickness
AR6	6Th Assessment Report
BCF	Black carbon volume fraction
BFGS	Broyden–Fletcher–Goldfarb–Shanno
CCL	Clear-sky confidence levels
CEOS	Committee on Earth Observation Satellites
CLAUDIA	CLoud and Aerosol Unbiased Decision Intellectual Algorithm
COCCON	COllaborative Carbon Column Observing Network
CONTRAIL	Comprehensive Observation Network for TRace gases by AirLiner project
CrIS	Cross-track infrared sounder
DFS	Degrees of freedom for signals
DIAL	Differential absorption lidar

DOE	Department of energy
EarthCARE	Earth clouds, aerosols and radiation explorer
ENVISAT	ENVironmental SATellite
ESRL/GMD	Earth System Research Laboratory/Global Monitoring Division
FLEX	FLUorescence explorer
fAPAR	Fraction of absorbed PAR
GEMS	Geostationary Environment Monitoring Spectrometer
GHG	Greenhouse gas
GOME	Global Ozone Monitoring Experiment
GOSAT	Greenhouse gases observing SATellite
GPP	Gross primary production
HITRAN	Hlgh-resolution TRANsmission molecular absorption
IAGOS	In-service Aircraft for a Global Observing System
IASI	Infrared Atmospheric Sounding Interferometer
IFOV	Instantaneous field of view
ILS	Instrument line shape
IPCC	Intergovernmental Panel on Climate Change
JMA	Japan Meteorological Agency
LBLRTM	Line-by-line radiative transfer model
LOS	Line of sight
LUE	Light use efficiency
MAP	Maximum a posteriori
MLI	Multilayer insulation
MOBY	Marine optical BuoY
MODIS	MODerate resolution Imaging Spectroradiometer
MOPITT	Measurements of Pollution In The Troposphere
MWPM	Multi-wavelength and multi-pixel method
NASA	National Aeronautics and Space Administration
NDACC	Network for the Detection of Atmospheric Composition Change
NDVI	Normalized difference vegetation index
NICAM	Nonhydrostatic ICosahedral Atmospheric Model
NICAM-TM	NICAM-based Transport Model
NISMON	NICAM-based Inverse Simulation for Monitoring
NOAA	National Oceanic and Atmospheric Administration
OCO	Orbiting Carbon Observatory
OECD	Organization for Economic Co-operation and Development
OMI	Ozone monitoring instrument
OMPS	Ozone Mapping and Profiler Suite
OSA	Optical spectrum analyzer
PAR	Photosynthetically active radiation
PFT	Pre-flight test
RGB	Red green and blue
RRV	RailRoad valley
RTes	Radiative transfer equations
SCIAMACHY	SCanning Imaging Absorption spectroMeter for Atmospheric CHartography
SCOPE	Sustained and COordinated Processing of Environmental satellite data
SIF	Solar-induced fluorescence
SLCF	Short-lived climate forcer
SNR	Signal-to-noise ratio
SSA	Single scattering albedo
SVM	Support vector machine
SWIR	Short wavelength InfraRed
TanSat	Chinese Carbon Dioxide Observation SATellite Mission
TANSO-CAI	Thermal and Near Infrared Sensor for carbon Observation-Cloud and Aerosol Imager
TANSO-FTS	Thermal and Near Infrared Sensor for carbon Observation-Fourier Transform Spectrometer
TCCON	The Total Carbon Column Observing Network
TEMPO	Tropospheric Emissions: Monitoring Pollution
TIR	Thermal InfraRed
TOA	Top of the atmosphere
TROPOMI	TROPOspheric Monitoring Instrument
UNFCCC	United Nations Framework Convention on Climate Change
UV	UltraViolet

VIIRS	Visible Infrared Imaging Radiometer Suite
VNIR	Visible and near InfraRed
WDCGG	World Data Center for Greenhouse Gases
WMO	World Health Organization

Acknowledgements

This research has been supported by the Ministry of Environment, Japan.

Author contributions

RI, TM, and MN proposed the topic and conceived the study. YY developed retrieval systems. KS carried out calibration of the sensors. IM and UO conducted validation study. NS and YS developed retrieval algorithms for TIR data. YN, SM, and HT developed the inverse analysis system. YO, HI, and TYN developed the cloud screening system. MH, TN, and CS developed the aerosol retrieval system and analyzed aerosol data. HN and KH analyzed SIF data. All authors read and approved the final manuscript.

Availability of data and materials

All standard products of GOSAT and GOSAT-2 project can be downloaded from the GOSAT Data Archive Service (GDAS) [<https://data2.gosat.nies.go.jp/>] and the GOSAT-2 Product Archive [<https://prdct.gosat-2.nies.go.jp/index.html.ja>].

Declarations

Competing interests

The authors declare that they have no competing interest.

Author details

¹ Atmosphere and Ocean Research Institute, The University of Tokyo, 5-1-5 Kashiwanoha, Kashiwa, Chiba 277-8568, Japan. ² National Institute for Environmental Studies, 16-2 Onogawa, Tsukuba, Ibaraki 305-8506, Japan. ³ Japan Aerospace Exploration Agency, 2-1-1 Sengen, Tsukuba, Ibaraki 305-8505, Japan. ⁴ Center for Environmental Remote Sensing (CEReS), Chiba University, 1-33 Yayoi-Cho, Inage-Ku, Chiba-Shi, Chiba 263-8522, Japan. ⁵ Tohoku University, Aoba, Sendai, Miyagi 980-8578, Japan. ⁶ Research Center for Agricultural Information Technology, The National Agriculture and Food Research Organization, 1-31-1 Kannondai, Tsukuba, Ibaraki 305-0856, Japan. ⁷ Meteorological Research Institute, Japan Meteorological Agency, 1-1 Nagamine, Tsukuba, Ibaraki 305-0052, Japan. ⁸ Tokai University, 2-28-4 Tomigaya, Shibuya, Tokyo 151-8677, Japan. ⁹ Aerospace Information Research Institute, Chinese Academy of Sciences, No.9 Dengzhuang South Road, Haidian District, Beijing 100094, China.

Received: 11 November 2022 Accepted: 6 June 2023

Published: 3 July 2023

References

- Baker NRX (2008) Chlorophyll fluorescence: a probe of photosynthesis in vivo. *Annual Rev Plant Biol* 59:89–113
- Beer R, Shephard MW, Kulawik SS, Clough SA, Eldering A, Bowman KW, Sander SP, Fisher BM, Payne VH, Luo M (2008) First satellite observations of lower tropospheric ammonia and methanol. *Geophys Res Lett* 35:L09801. <https://doi.org/10.1029/2008GL033642>
- Biraud SC, Torn MS, Smith JR, Sweeney C, Riley WJ, Tans PP (2013) A multi-year record of airborne CO₂ observations in the US Southern Great Plains. *Atmos Meas Tech* 6:751–763. <https://doi.org/10.5194/amt-6-751-2013>
- Boesch H, Deutscher NM, Warneke T, Byckling K, Cogan AJ, Griffith DW, Notholt J, Parker RJ, Wang Z (2013) HDO/H₂O ratio retrievals from GOSAT. *Atmos Meas Tech* 6:599–612. <https://doi.org/10.5194/amt-6-599-2013>
- Clerbaux C, Boynard A, Clarisse L, George M, Hadji-Lazaro J, Herbin H, Hurtmans D, Pommier M, Razavi A, Turquety S (2009) Monitoring of atmospheric composition using the thermal infrared IASI/MetOp sounder. *Atmos Chem Phys* 9:6041–6054
- Clough SA, Shephard MW, Mlawer EJ, Delamere JS, Iacono MJ, Cady-Pereira K, Boukabara S, Brown PD (2005) Atmospheric radiative transfer modeling: a summary of the AER codes. *J Quant Spectr Radiat Trans* 91:233–244
- Coheur PF, Clarisse L, Turquety S, Hurtmans D, Clerbaux C (2009) IASI measurements of reactive trace species in biomass burning plumes. *Atmos Chem Phys* 9:5655–5667
- Crisp D, Pollock HR, Rosenberg R, Chapsky L, Lee RAM, Oyafuso FA, Frankenberg C, O'Dell CW, Bruegge CJ, Doran GB, Eldering A, Fisher BM, Fu D, Gunson MR, Mandrake L, Osterman GB, Schwandner FM, Sun K, Taylor TE, Wennberg PO, Wunch D (2017) The on-orbit performance of the Orbiting Carbon Observatory-2 (OCO-2) instrument and its radiometrically calibrated products. *Atmos Meas Tech* 10:59–81. <https://doi.org/10.5194/amt-10-59-2017>
- Daughtry CST, Walthall CL, Kim MS, Brown de Colstoun E, McMurtrey JE (2000) Estimating corn leaf chlorophyll concentration from leaf and canopy reflectance. *Remote Sens Env* 74:229–239
- De Mazière M, Thompson AM, Kurylo MJ, Wild JD, Bernhard G, Blumenstock T, Braathen GO, Hannigan JW, Lambert J-C, Leblanc T, McGee TJ, Nedoluha G, Petropavlovskikh I, Seckmeyer G, Simon PC, Steinbrecht W, Strahan SE (2018) The Network for the Detection of Atmospheric Composition Change (NDACC): history, status and perspectives. *Atmos Chem Phys* 18:4935–4964. <https://doi.org/10.5194/acp-18-4935-2018>
- Du S, Liu L, Liu X, Zhang X, Zhang X, Bi Y, Zhang, (2018) Retrieval of global terrestrial solar-induced chlorophyll fluorescence from TanSat satellite. *Sci Bull* 63:1502–1512. <https://doi.org/10.1016/j.scib.2018.10.003>
- Eldering A, Taylor TE, O'Dell CW, Pavlick P (2019) The OCO-3 mission: measurement objectives and expected performance based on 1 year of simulated data. *Atmos Meas Tech* 12:2341–2370. <https://doi.org/10.5194/amt-12-2341-2019>
- Filges A, Gerbig C, Chen H, Franke H, Klaus C, Jordan A (2015) The IAGOS-core greenhouse gas package: a measurement system for continuous airborne observations of CO₂, CH₄, H₂O and CO. *Tellus B* 67:27989. <https://doi.org/10.3402/tellusb.v67.27989>
- Frankenberg C, Aben I, Bergamaschi P, Dlugokencky EJ, van Hees R, Houweling S, van der Meer P, Snel R, Tol P (2011a) Global column-averaged methane mixing ratios from 2003 to 2009 as derived from SCIAMACHY: Trends and variability. *J Geophys Res* 116:D04302. <https://doi.org/10.1029/2010JD014849>
- Frankenberg C, Butz A, Toon GC (2011b) Disentangling chlorophyll fluorescence from atmospheric scattering effects in O₂ A-band spectra of reflected sun-light. *Geophys Res Lett* 38:L1–5
- Frankenberg C, Fisher JB, Worden J, Badgley G, Saatchi SS, Lee JE, Toon GC, Butz A, Jung M, Kuze A, Yokota T (2011c) New global observations of the terrestrial carbon cycle from GOSAT: patterns of plant fluorescence with gross primary productivity. *Geophys Res Lett* 38:L17706. <https://doi.org/10.1029/2011GL048738>
- Frankenberg C, O'Dell C, Gunter L, McDuffie J (2012) Remote sensing of near-infrared chlorophyll fluorescence from space in scattering atmospheres: implications for its retrieval and interferences with atmospheric CO₂ retrievals. *Atmos Meas Tech* 5:2081–2094
- Frey M, Sha MK, Hase F, Kiel M, Blumenstock T, Harig R, Surawicz G, Deutscher NM, Shiomi K, Franklin JE, Bösch H, Chen J, Grutter M, Ohyama H, Sun Y, Butz A, Mengistu Tsidu G, Ene D, Wunch D, Cao Z, Garcia O, Ramonet M, Vogel F, Orphal J (2019) Building the CO₂ Collaborative Carbon Column Observing Network (COCCON): long-term stability and ensemble performance of the EM27/SUN Fourier transform spectrometer. *Atmos Meas Tech* 12:1513–1530. <https://doi.org/10.5194/amt-12-1513-2019>
- Fujii Y (2005) Preconditioned optimizing utility for large-dimensional analyses (POpULar). *J Oceanogr* 61:167–181. <https://doi.org/10.1007/s10872-005-0029-z>
- Fujinawa T, Kuze A, Suto H, Shiomi K, Kanaya Y, Kawashima T, Kataoka F, Mori S, Eskes H, Tanimoto H (2021) First concurrent observations of NO₂ and CO₂ from power plant plumes by airborne remote sensing. *Geophys Res Lett*. <https://doi.org/10.1029/2021GL092685>
- Fukuda S, Nakajima T, Takenaka H, Higurashi A, Kikuchi N, Nakajima TY, Ishida H (2013) New approaches to removing cloud shadows and evaluating the 380 nm surface reflectance for improved aerosol optical thickness retrievals from the GOSAT/TANSO-Cloud and Aerosol Imager. *J Geophys Res* 118:13–520. <https://doi.org/10.1002/2013JD020090>
- Garzonio R, Di Mauro B, Colombo R, Cogliati S (2017) Surface reflectance and sun-induced fluorescence spectroscopy measurements using a small hyperspectral UAS. *Remote Sens* 9:472. <https://doi.org/10.3390/rs9050472>

- Global Carbon Project (2017) Supplemental data of Global Carbon Budget 2017 (Ver 1.0). Global Carbon Project. <https://doi.org/10.18160/gcp-2017>
- Gogoi MM, Babu SS, Imasu R, Hashimoto M (2022) Satellite (GOSAT-2 CAI-2) retrieval and surface (ARFINET) observations of Aerosol Black Carbon over India. *Atmos Chem Phys Discuss*. <https://doi.org/10.5194/acp-2022-555>
- Gogoi MM, Babu SS, Imasu R, Hashimoto H (2021) Aerosol black carbon over India from satellite (GOSAT-2 CAI-2) and ground-based (ARFINET) measurements. In: Abstract of the International SKYNET Workshop, Chiba, 9–12 Nov 2021
- Goldberg DL, Lu Z, Oda T, Lamsal LN, Liu F, Griffin D, McLinden CA, Krotkov NA, Duncan BN, Streets DG (2019) Exploiting OMI NO₂ satellite observations to infer fossil-fuel CO₂ emissions from US megacities. *Sci Total Environ*. <https://doi.org/10.1016/j.scitotenv.2019.133805>
- Guanter L, Frankenberg C, Dudhia A, Lewis PE, Gomez-Dans J, Kuze A, Suto H, Franer RG (2012) Retrieval and global assessment of terrestrial chlorophyll fluorescence from GOSAT space measurements. *Remote Sens Environ* 121:236–251
- Guanter L, Zhang Y, Jung M, Joiner J, Voigt M, Berry JA, Frankenberg C, Huete AR, Zarco-Tejada P, Lee JE, Moran MS, Ponce-Campos G, Beer C, Camps-Valls G, Buchmann N, Gianelle D, Klumpp K, Cescatti A, Baker JM, Griffis TJ (2014) Global and time-resolved monitoring of crop photosynthesis with chlorophyll fluorescence. *Nati Acad Sci USA* 111:E1327–1333. <https://doi.org/10.1073/pnas.1320008111>
- Guanter L, Aben I, Tol P, Krijger JM, Hollstein A, Köhler P, Damm A, Joiner J, Frankenberg C, Landgraf J (2015) Potential of the TROPospheric Monitoring Instrument (TROPOMI) onboard the Sentinel-5 Precursor for the monitoring of terrestrial chlorophyll fluorescence. *Atmos Meas Tech* 8:1337–1352
- Guerlet S, Butz A, Schepers D, Basu S, Hasekamp OP, Kuze A, Yokota T, Blavier J-F, Deutscher NM, Griffith DW, Hase F, Kyrö E, Morino I, Sherlock V, Sussmann R, Galli A, Aben I (2013) Impact of aerosol and thin cirrus on retrieving and validating XCO₂ from GOSAT shortwave infrared measurements. *J Geophys Res* 118:4887–4905
- Hamazaki T, Kaneko Y, Kuze A, Kondo K (2005) Fourier transform spectrometer for Greenhouse Gases Observing Satellite (GOSAT). *Proc SPIE* 5659:73
- Hashimoto M, Nakajima T (2017) Development of a remote sensing algorithm to retrieve atmospheric aerosol properties using multi-wavelength and multi-pixel information. *J Geophys Res*. <https://doi.org/10.1002/2016JG0025698>
- Hikosaka K, Tsujimoto K (2021) Linking remote sensing parameters to CO₂ assimilation rates at a leaf scale. *J Plant Res* 134:695–711. <https://doi.org/10.1007/s10265-021-01313-4>
- Imasu R (2019) Expected scientific achievement by GOSAT-2 Science plan. *J Remo Sens Soc Jpn* 39:9–13. <https://doi.org/10.11440/rssj.39.9>
- Inoue T (1985) On the temperature and effective emissivity determination of semi-transparent cirrus clouds by bi-spectral measurements in the 10 mm window region. *J Meteor Soc Jpn* 63:88–99
- Inoue M, Morino I, Uchino O, Miyamoto Y, Yoshida Y, Yokota T, Machida T, Sawa Y, Matsueda H, Sweeney C, Tans PP, Andrews AE, Biraud SC, Tanaka T, Kawakami S, Patra PK (2013) Validation of XCO₂ derived from SWIR spectra of GOSAT TANSO-FTS with aircraft measurement data. *Atmos Chem Phys* 13:9771–9788. <https://doi.org/10.5194/acp-13-9771-2013>
- Inoue M, Morino I, Uchino O, Nakatsuru T, Yoshida Y, Yokota T, Wunch D, Wennberg PO, Roehl CM, Griffith DWT, Velasco VA, Deutscher NM, Warneke T, Notholt J, Robinson J, Sherlock V, Hase F, Blumenstock T, Rettinger M, Sussmann R, Kyrö E, Kivi R, Shiomi K, Kawakami S, De Mazière M, Arnold SG, Feist DG, Barrow EA, Barney J, Dubey M, Schneider M, Iraqi LT, Podolske JR, Hillyard PW, Machida T, Sawa Y, Tsuboi K, Matsueda H, Sweeney C, Tans PP, Andrews AE, Biraud SC, Fukuyama Y, Pittman JV, Kort EA, Tanaka T (2016) Bias corrections of GOSAT SWIR XCO₂ and XCH₄ with TCCON data and their evaluation using aircraft measurement data. *Atmos Meas Tech* 9:3491–3512. <https://doi.org/10.5194/amt-9-3491-2016>
- Intergovernmental Panel on Climate Change (2018) Global Warming of 1.5°C. <https://www.ipcc.ch/sr15/>. Accessed 25 Sept 2022
- Intergovernmental Panel on Climate Change (2021) Climate Change 2021: The Physical Science Basis. Cambridge University Press, UK
- Ishida H, Nakajima TY (2009) Development of an unbiased cloud detection algorithm for a spaceborne multispectral imager. *J Geophys Res* 114:D07206
- Ishida H, Oishi Y, Morita K, Moriwaki K, Nakajima TY (2018) Development of a support vector machine based cloud detection method for MODIS with the adjustability to various conditions. *Remote Sens Environ* 205:390–407. <https://doi.org/10.1016/j.rse.2017.11.003>
- Ishijima K, Patra PK, Takigawa M, Machida T, Matsueda H, Sawa Y, Steele LP, Krummel PB, Langenfelds RL, Aoki S, Nakazawa T (2010) Stratospheric influence on the seasonal cycle of nitrous oxide in the troposphere as deduced from aircraft observations and model simulations. *J Geophys Res* 115:D20308. <https://doi.org/10.1029/2009JD013322>
- Itahashi S, Yumimoto K, Kurokawa J, Morino Y, Nagashima T, Miyazaki K, Maki T, Ohara T (2019) Inverse estimation of NO_x emissions over China and India 2005–2016: contrasting recent trends and future perspectives. *Environ Res Lett* 14:124020. <https://doi.org/10.1088/1748-9326/ab4d7f>
- Japan Aerospace Exploration Agency (2020) Large scale Australian forest fire observed from space, Earthview. <https://www.eorc.jaxa.jp/earthview/2020/tp200131.html>. Accessed 25 Sept 2022
- Jethva H, Torres O (2019) A comparative evaluation of Aura-OMI and SKYNET near-UV single-scattering albedo products. *Atmos Meas Tech* 12:6489–6503. <https://doi.org/10.5194/amt-12-6489-2019>
- Joiner J, Yoshida Y, Vasilkov AP, Yoshida Y, Corp LA, Middleton EM (2011) First observations of global and seasonal terrestrial chlorophyll fluorescence from space. *Biogeosciences* 8:637–651
- Joiner J, Yoshida Y, Vasilkov AP, Middleton EM, Campbell PKE, Yoshida Y, Kuze A, Corp LA (2012) Filling-in of near-infrared solar lines by terrestrial fluorescence and other geophysical effects: simulations and space-based observations from SCIAMACHY and GOSAT. *Atmos Meas Tech* 5:809–829
- Joiner J, Guanter L, Lindstrot R, Voigt M, Vasilkov AP, Middleton EM, Huemrich KF, Yoshida Y, Frankenberg C (2013) Global monitoring of terrestrial chlorophyll fluorescence from moderate-spectral-resolution near-infrared satellite measurements: methodology, simulations, and application to GOME-2. *Atmos Meas Tech* 6:2803–2823. <https://doi.org/10.5194/amt-6-2803-2013>
- Julitta T, Corp LA, Rossini M, Burkart A, Cogliati S, Davies N, Hom M, Mac Arthur A, Middleton EM, Rascher U, Schickling A, Colombo R (2016) Comparison of Sun-induced chlorophyll fluorescence estimates obtained from four portable field spectroradiometers. *Remote Sens* 8:122. <https://doi.org/10.3390/rs8020122>
- Karion A, Sweeney C, Tans P, Newberger T (2010) AirCore: an innovative atmospheric sampling system. *J Atmos Ocean Tech* 27:1839–1853. <https://doi.org/10.1175/2010JTECHA1448.1>
- Kaufman YJ (1987) Satellite sensing of aerosol absorption. *J Geophys Res* 92:4307–4317. <https://doi.org/10.1029/JD092iD04p04307>
- Kawasaki M, Yoshioka H, Jones NB, Macatangay R, Griffith DWT, Kawakami S, Ohyama H, Tanaka T, Morino I, Uchino O, Ibuki T (2012) Usability of optical spectrum analyzer in measuring atmospheric CO₂ and CH₄ column densities: inspection with FTS and aircraft profiles in situ. *Atmos Meas Tech* 5:2593–2600. <https://doi.org/10.5194/amt-5-2593-2012>
- Kim J, Jeong U, Ahn MH, Kim JH, Park RJ, Lee H, Song CH, Choi YS, Lee KH, Yoo JM, Jeong MJ, Park SK, Lee KM, Song CK, Kim SW, Kim YJ, Kim SW, Kim M, Go S, Liu X, Chance K, Miller CC, Al-Saadi J, Veihelmann B, Bhartia PK, Torres O, Abad GG, Haffner DP, Ko DH, Lee SH et al (2020) New era of air quality monitoring from space: geostationary environment monitoring spectrometer (GEMS). *Bull Amer Meteor Soc* 101:E1–E22. <https://doi.org/10.1175/BAMS-D-18-0013.1>
- Kobayashi N, Inoue G, Kawasaki M, Yoshioka H, Minomura M, Murata I, Nagahama T, Matsumi Y, Tanaka T, Morino I, Ibuki T (2010) Remotely operable compact instruments for measuring atmospheric CO₂ and CH₄ column densities at surface monitoring sites. *Atmos Meas Tech* 3:1103–1112. <https://doi.org/10.5194/amt-3-1103-2010>
- Köhler P, Frankenberg C, Magney TS, Guanter L, Joiner J, Landgraf J (2018) Global retrievals of solar induced chlorophyll fluorescence with TROPOMI: first results and inter-sensor comparison to OCO-2. *Geophys Res Lett* 45:10456–10463. <https://doi.org/10.1029/2018GL079031>
- Kuze A, Suto H, Nakajima M, Hamazaki T (2009) Thermal and near infrared sensor for carbon observation Fourier-transform spectrometer on the Greenhouse Gases Observing Satellite for greenhouse gases monitoring. *Appl Opt* 48:6716–6733. <https://doi.org/10.1364/AO.48.006716>
- Lee JE, Frankenberg C, van der Tol C, Berry JA, Guanter L, Boyce CK, Fisher JB, Morrow E, Worden JR, Asefi S, Badgley G, Saatchi S (2013) Forest productivity and water stress in Amazonia: observations from GOSAT

- chlorophyll fluorescence. *Royal Soci b: Bio Sci* 280:20130171–20130171. <https://doi.org/10.1098/rspb.2013.0171>
- Liu J, Bowman KW, Schimel DS, Parazoo NC, Jiang Z, Lee M, Bloom AA, Wunch D, Frankenberg C, Sun Y, O'Dell CW, Gurney KR, Menemenlis D, Gierach M, Crisp D, Eldering A (2017) Contrasting carbon cycle responses of the tropical continents to the 2015–2016 El Niño. *Science* 358:aa5690
- Machida T, Matsueda H, Sawa Y, Nakagawa Y, Hirofumi K, Kondo N, Goto K, Nakazawa T, Ishikawa T, Ogawa T (2008) Worldwide measurements of atmospheric CO₂ and other trace gas species using commercial airlines. *J Atmos Ocean Tech* 25:1744–1754. <https://doi.org/10.1175/2008JTECHA1082.1>
- Meroni M, Rossini M, Guanter L, Alonsoc L, Rascher U, Colombo R, Moreno J (2009) Remote sensing of solar-induced chlorophyll fluorescence: review of methods and applications. *Remo Sens Env* 113:2037–2051. <https://doi.org/10.1016/j.rse.2009.05.003>
- Migliavacca M, Perez-Priego O, Rossini M, El-Madany TS, Moreno G, van der Tol C, Rascher U, Berninger A, Bessenbacher V, Burkart A, Carrara A, Fava F, Guan JH, Hammer TW, Henkel K, Juarez-Alcalde E, Julitta T, Kolle O, Martin MP, Musavi T, Pacheco-Labrador J, Perez-Burgueno A, Wutzler T, Zaehle S, Reichstein M (2017) Plant functional traits and canopy structure control the relationship between photosynthetic CO₂ uptake and far-red sun-induced fluorescence in a Mediterranean grassland under different nutrient availability. *New Phytol* 214:1078–1091. <https://doi.org/10.1111/nph.14437>
- Monteith JL (1972) Solar radiation and productivity in tropical ecosystems. *J App Ecology* 9:747–766
- Nakajima T (2021) Development of earth observation satellites for the atmospheric sciences. *J Remote Sens Soc Jpn* 41:109–118
- Nakajima T, Tanaka M (1986) Matrix formulation for the transfer of solar radiation in a plane-parallel scattering atmosphere. *J Quant Spect Rad Trans* 35:13–21
- Nakajima T, Tanaka M (1988) Algorithms for radiative intensity calculations in moderately thick atmospheres using a truncation approximation. *J Quant Spect Rad Trans* 40:51–69
- Nakajima T, Ohara T, Masui T, Takemura T, Yoshimura K, Goto D, Hanaoka T, Itahashi S, Kurata G, Kurokawa J, Maki T, Masutomi Y, Nakata M, Nitta T, Seposo X, Sudo K, Suzuki C, Suzuki K, Tsuruta H, Ueda K, Watanabe S, Yu Y, Yumimoto K, Zhao S (2020a) A development of reduction scenarios of the short-lived climate pollutants (SLCPs) for mitigating global warming and environmental problems. *Prog Earth Planet Sci* 7:33. <https://doi.org/10.1186/s40645-020-00351-1>
- Nakajima T, Campanelli M, Che H, Estellés V, Irie H, Kim S-W, Kim J, Liu D, Nishizawa T, Pandithurai G, Soni VK, Thana B, Tugjurn N-U, Aoki K, Go S, Hashimoto M, Higurashi A, Kazadzis S, Khatri P, Kouremeti N, Kudo R, Marengo F, Momoi M, Ningombam SS, Ryder CL, Uchiyama A, Yamazaki A (2020b) An overview of and issues with sky radiometer technology and SKYNET. *Atmos Meas Tech* 13:4195–4218. <https://doi.org/10.5194/amt-13-4195-2020>
- Nguyen H, Osterman G, Wunch D, O'Dell C, Mandrake L, Wennberg P, Fisher B, Castano R (2014) A method for collocating satellite XCO₂ data to ground-based data and its application to ACOS-GOSAT and TCCON. *Atmos Meas Tech* 7:2631–2644. <https://doi.org/10.5194/amt-7-2631-2014>
- Niwa Y, Fujii Y (2020) A conjugate BFGS method for accurate estimation of a posterior error covariance matrix in a linear inverse problem. *Quart J Royal Meteorol Soc* 146:3118–3143. <https://doi.org/10.1002/qj.3838>
- Niwa Y, Tomita H, Satoh M, Imasu R (2011) A three-dimensional icosahedral grid advection scheme preserving monotonicity and consistency with continuity for atmospheric tracer transport. *J Meteor Soc Jpn* 89:255–268
- Niwa Y, Tomita H, Satoh M, Imasu R, Sawa Y, Tsuboi K, Matsueda H, Machida T, Sasakawa M, Belan B, Saigusa N (2017a) A 4D-Var inversion system based on the icosahedral grid model (NICAM-TM 4D-Var v1.0)—part 1: offline forward and adjoint transport models. *Geosci Model Dev* 10:1157–1174. <https://doi.org/10.5194/gmd-10-1157-2017>
- Niwa Y, Fujii Y, Sawa Y, Iida Y, Ito A, Satoh M, Imasu R, Tsuboi K, Matsueda H, Saigusa N (2017b) A 4D-Var inversion system based on the icosahedral grid model (NICAM-TM 4D-Var v1.0)—part 2: optimization scheme and identical twin experiment of atmospheric CO₂ inversion. *Geosci Model Dev* 10:2201–2219. <https://doi.org/10.5194/gmd-10-2201-2017>
- Ohyama H, Kawakami S, Shiomi K, Morino I, Uchino O (2013) Atmospheric temperature and water vapor retrievals from GOSAT thermal infrared spectra and initial validation with coincident radiosonde measurements. *SOLA* 9:143–147
- Oishi Y, Nagao T, Ishida H, Nakajima TY, Matsunaga T (2015) Preliminary study of a method using the GOSAT-2 CAI-2 cloud discrimination for screening of cloud-contaminated FTS-2 data. *J Remote Sens Soc Jpn* 35:299–306
- Oishi Y, Nakajima TY, Matsunaga T (2016) Difference between forward- and backward-looking bands of GOSAT-2 CAI-2 cloud discrimination used with Terra MISR data. *Int J Remote Sens* 37:1115–1126
- Oishi Y, Ishida H, Nakamura R, Matsunaga T (2017) The impact of different support vectors on GOSAT-2 CAI-2 L2 Cloud discrimination. *Remote Sens* 9:1236. <https://doi.org/10.3390/rs9121236>
- Oishi Y, Ishida H, Nakajima TY, Nakamura R, Matsunaga T (2018) Preliminary verification for application of a support vector machine-based cloud detection method to GOSAT-2 CAI-2. *Atmos Meas Tech* 11:2863–2878. <https://doi.org/10.5194/amt-11-2863-2018>
- Organisation for Economic Co-operation and Development (2020) Environment at a glance 2020. OECD Publishing, Paris. <https://doi.org/10.1787/4ea7d35f-en>
- Oshio H, Yoshida Y, Matsunaga T (2019) On the zero-level offset in the GOSAT TANSO-FTS O2 A band and the quality of solar-induced chlorophyll fluorescence (SIF): comparison of SIF between GOSAT and OCO-2. *Atmos Meas Tech* 12:6721–6735. <https://doi.org/10.5194/amt-12-6721-2019>
- Ouchi M, Matsumi Y, Nakayama T, Shimizu K, Sawada T, Machida T, Matsueda H, Sawa Y, Morino I, Uchino O, Tanaka T, Imasu R (2019) Development of a balloon-borne instrument for CO₂ vertical profile observations in the troposphere. *Atmos Meas Tech* 12:5639–5653. <https://doi.org/10.5194/amt-12-5639-2019>
- Parazoo NC, Bowman K, Frankenberg C, Lee JE, Fisher JB, Worden J, Jones DBA, Berry J, Collatz GJ, Baker IT, Jung M, Liu J, Osterman G, O'Dell C, Sparks A, Butz A, Guerlet S, Yoshida Y, Chen H, Gerbig C (2013) Interpreting seasonal changes in the carbon balance of southern Amazonia using measurements of XCO₂ and chlorophyll fluorescence from GOSAT. *Geophys Res Lett* 40:2829–2833
- Parazoo NC, Bowman K, Fisher JB, Frankenberg C, Jones DBA, Cescatti A, Pérez-Priego O, Wohlfahrt G, Montagnani L (2014) Terrestrial gross primary production inferred from satellite fluorescence and vegetation models. *Global Change Biol* 20:3103–3121
- Parker R, Boesch H, Cogan A, Fraser A, Feng L, Palmer PI, Messerschmidt J, Deutscher N, Griffith DWT, Notholt J, Wennberg PO, Wunch D (2011) Methane observations from the Greenhouse Gases Observing Satellite: Comparison to ground-based TCCON data and model calculations. *Geophys Res Lett* 38:L15807. <https://doi.org/10.1029/2011GL047871>
- Porcar-Castell A, Tyystjärvi E, Atherton J, van der Tol C, Flexas J, Pfündel EE, Moreno J, Frankenberg C, Berry JA (2014) Linking chlorophyll *a* fluorescence to photosynthesis for remote sensing applications: mechanisms and challenges. *J Exp Bot* 65:4065–4095
- Rodgers CD (2000) Inverse methods for atmospheric sounding: theory and practice. World Science, Singapore
- Rothman LS, Jacquemart D, Barbe A, Benner DC, Birk M, Brown L, Carleer M, Chackerian C, Chance KLH, Dana V, Devi VM, Flaud JM, Gamache RR, Goldman A, Hartmann JM, Jucks KW, Maki AG, Mandin JY, Massie ST, Orphal J, Perrin A, Rinsland CP, Smith MAH, Tennyson J, Tolchenov RN, Toth RA, Vander Auwera J, Varanasi P, Wagner G (2005) The HITRAN 2004 molecular spectroscopic database. *J Quant Spect Rad Trans* 96:139–204
- Rothman LS, Gordon IE, Barbe A, Benner DC, Bernath PF, Birk M, Boudon V, Brown LR, Campargue A, Champion JP, Chance K, Coudert LH, Dana V, Devi VM, Fally S, Flaud J-M, Gamache RR, Goldman A, Jacquemart D, Kleiner I, Lacombe N, Lafferty WJ, Mandin J-Y, Massie ST, Mikhailenko SN, Miller CE, Moazzen-Ahmadi N, Naumenko OV, Nikitin AV, Orphal J, Perevalov VI, Perrin A, Predoi-Cross A, Rinsland CP, Rotger M, Simeckova M, Smith MAH, Sung K, Tashkun SA, Tennyson J, Toth RA, Vandaele AC, Vander Auwera J (2009) The HITRAN 2008 molecular spectroscopic database. *J Quant Spect Rad Trans* 110:533–572
- Rothman L, Gordon I, Babikov Y, Barbe A, Benner DC, Bernath P, Birk M, Bizzocchi L, Boudon V, Brown LR, Campargue A, Chance K, Coudert LH, Devi VM, Drouin BJ, Fayt A, Flaud J-M, Gamache RR, Harrison JJ, Hartmann J-M, Hill C, Hodges JT, Jacquemart D, Jolly A, Lamouroux J, Le Roy RJ,

- Li G, Long DA, Lyulin ST, Mackie OM, Massie ST, Mikhailenko S, Muller HSP, Naumenko OV, Nikitin AV, Orphal J, Perevalov V, Perrin A, Polotseva ER, Richard C, Smith MAH, Starikova E, Sung K, Tashkun SA, Tennyson J, Toon GC, VIG T, Wagner G (2013) The HITRAN2012 molecular spectroscopic database. *J Quant Spectr Rad Trans* 130:4–50
- Running SW, Nemani R, Heinsch FA, Zhao RM, Hashimoto H (2004) A continuous satellite-derived measure of global terrestrial primary production. *Biosci* 54:547–560
- Saito M, Niwa Y, Saeki T, Cong R, Miyauchi T (2019) Overview of model systems for global carbon dioxide and methane flux estimates using GOSAT and GOSAT-2 observations. *J Remo Sens Soc Japan* 39:50–56
- Saitoh N, Imasu R, Ota Y, Niwa Y (2009) CO₂ retrieval algorithm for the thermal infrared spectra of the greenhouse gases observing satellite potential of retrieving CO₂ vertical profile from high-resolution FTS sensor. *J Geophys Res*. <https://doi.org/10.1029/2007JD011500>
- Saitoh N, Kimoto S, Sugimura R, Imasu R, Kawakami S, Shiomi K, Kuze K, Machia T, Sawa Y, Matsueda H (2016) Algorithm update of the GOSAT/TANSO-FTS thermal infrared CO₂ product (version 1) and validation of the UTLS CO₂ data using CONTRAIL measurements. *Atmos Meas Tech* 9:2119–2134
- Sakaizawa D, Nagasawa C, Nagai T, Abo M, Shibata Y, Nakazato M, Sakai T (2009) Development of a 1.6 μm differential absorption lidar with a quasi-phase matching OPO and photon-counting detector for the vertical CO₂ profile. *Appl Opt* 48:748–757. <https://doi.org/10.1364/AO.48.000748>
- Satoh M, Tomita H, Yashiro H, Miura H, Kodama C, Seiki T, Noda AT, Yamada Y, Goto D, Sawada M, Miyoshi T, Niwa Y, Hara M, Ohno T, Iga S, Arakawa T, Inoue T, Kubokawa H (2014) The non-hydrostatic icosahedral atmospheric model: description and development. *Prog Earth Planet Sci* 1:18. <https://doi.org/10.1186/s40645-014-0018-1>
- Schmid B, Tomlinson JM, Hubbe JM, Comstock JM, Mei F, Chand D, Pekour MS, Kluzek CD, Andrews E, Biraud SC, McFarquhar GM (2014) The DOE ARM aerial facility. *Bull Am Meteor Soc* 95:723–742. <https://doi.org/10.1175/BAMS-D-13-00040.1>
- Sekiguchi M, Nakajima T (2008) A k-distribution-based radiation code and its computational optimization for an atmospheric general circulation model. *J Quant Spectr Rad Trans* 109:2779–2793. <https://doi.org/10.1016/j.jqsrt.2008.07.013>
- Shi C, Nakajima T (2018) Simultaneous determination of aerosol optical thickness and water-leaving radiance from multispectral measurements in coastal waters. *Atmos Chem Phys* 18:3865–3994
- Shi C, Hashimoto M, Nakajima T (2019) Remote sensing of aerosol properties from multi-wavelength and multi-pixel information over the ocean. *Atmos Chem Phys* 19:2461–2475
- Shi C, Hashimoto M, Shiomi K, Nakajima T (2020) Development of an algorithm to retrieve aerosol optical properties over water using an artificial neural network radiative transfer scheme: first result from GOSAT-2/CAI-2. *IEEE Trans Geosci Remote Sens*. <https://doi.org/10.1109/TGRS.2020.3038892>
- Someya Y, Imasu R, Saitoh N, Ota Y, Shiomi K (2016) A development of cloud top height retrieval using thermal infrared spectra observed with GOSAT and comparison with CALIPSO data. *Atmos Meas Tech* 9:1981–1992. <https://doi.org/10.5194/amt-9-1981-2016>
- Someya Y, Imasu R, Shiomi K (2019) Dust aerosol detection by the modified CO₂ slicing method. *Sensors* 19:1615. <https://doi.org/10.3390/s19071615>
- Someya Y, Imasu R, Shiomi K, Saitoh N (2020) Atmospheric ammonia retrieval from the TANSO-FTS/GOSAT thermal infrared sounder. *Atmos Meas Tech* 13:309–321. <https://doi.org/10.5194/amt-13-309-2020>
- Stohl A, Aamaas B, Amann M, Baker LH, Bellouin N, Berntsen TK, Boucher O, Cherian R, Collins W, Daskalakis N, Dusanakis M, Eckhardt S, Fuglestedt JS, Harju M, Heyes C, Hodnebrog Ø, Hao J, Im U, Kanakidou M, Klimont Z, Kupiainen K, Law KS, Lund MT, Maas R, MacIntosh CR, Myhre G, Myriokefalitakis S, Olivieri D, Quaas J, Quennehen B, Raut JC, Rumbold ST, Samset BH, Schulz M, Seland Ø, Shine KP, Skeie RB, Wang S, Yttri KE, Zhu T (2015) Evaluating the climate and air quality impacts of short-lived pollutants. *Atmos Chem Phys* 15:10529–10566
- Sun Y, Frankenberg C, Wood JD, Schimel DS, Jung M, Guanter L, Drewry DT, Verma M, Porcar-Castell A, Griffiths TJ, Gu L, Magney TS, Köhler P, Evans B, Yuen K (2017) OCO-2 advances photosynthesis observation from space via solar-induced chlorophyll fluorescence. *Science* 358:eam5747
- Suto H, Kataoka F, Kikuchi N, Knuteson RO, Butz A, Haun M, Buijs H, Shiomi K, Imai H, Kuze A (2021) Thermal and near-infrared sensor for carbon observation Fourier transform spectrometer-2 (TANSO-FTS-2) on the Greenhouse gases Observing SATellite-2 (GOSAT-2) during its first year in orbit. *Atmos Meas Tech* 14:2013–2039. <https://doi.org/10.5194/amt-14-2013-2021>
- Suto H, Kataoka F, Knuteson OR, Shiomi K, Kikuchi N, Kuze A (2022) Updated spectral radiance calibration on TIR bands for TANSO-FTS-2 onboard GOSAT-2. *Atmos Meas Tech* 15:5399–5413. <https://doi.org/10.5194/amt-15-5399-2022>
- Sweeney C, Karion A, Wolter S, Newberger T, Guenther D, Higgs JA, Andrews AE, Lang PM, Neff D, Dlugokencky E, Miller JB, Montzka SA, Miller BR, Masarie KA, Biraud SC, Novelli PC, Croftwell M, Croftwell AM, Thoning K, Tans PP (2015) Seasonal climatology of CO₂ across North America from aircraft measurements in the NOAA/ESRL global greenhouse gas reference network. *J Geophys Res* 120:5155–5190. <https://doi.org/10.1002/2014JD022591>
- Takagi H, Saeki T, Oda T, Saito M, Calsala V, Delikov D, Saito R, Yoshida Y, Morino I, Uchino O, Andres RJ, Yokota T, Maksyutov S (2011) On the benefit of GOSAT observations to the estimation of regional CO₂ fluxes. *SOLA* 7:161–164. <https://doi.org/10.2151/sola.2011-041>
- Takekawa N, Kondo Y, Koike M, Chen G, Machida T, Watai T, Blake DR, Streets DG, Woo JH, Carmichael GR, Kita K, Miyazaki Y, Shirai T, Liley JB, Ogawa T (2004) Removal of NO_x and NO_y in Asian outflow plume: Aircraft measurements over the western Pacific in January 2002. *J Geophys Res* 109:D23504. <https://doi.org/10.1029/2004JD004866>
- Takemura T, Suzuki K (2019) Weak global warming mitigation by reducing black carbon emissions. *Sci Rep* 9:4419. <https://doi.org/10.1038/s41598-019-41181-6>
- Takenaka H, Nakajima TY, Higurashi A, Higuchi A, Takamura T, Pinker RT, Nakajima T (2011) Estimation of solar radiation using a neural network based on radiative transfer. *J Geophys Res* 116:D08215. <https://doi.org/10.1029/2009JD013337>
- Thum T, Zaehle S, Köhler P, Aalto T, Aurela M, Guanter L, Kolari P, Laurila T, Lohila A, Magnani F, Van der Tol C, Markkanen T (2017) Modelling sun-induced fluorescence and photosynthesis with a land surface model at local and regional scales in northern Europe. *Biogeosci* 14:1969–1984
- Torres O, Jethva H, Ahn C, Jaross G, Loyola DG (2020) TROPOMI aerosol products: evaluation and observations of synoptic-scale carbonaceous aerosol plumes during 2018–2020. *Atmos Meas Tech* 13:6789–6806. <https://doi.org/10.5194/amt-13-6789-2020>
- Uchino O, Sakai T, Izumi T, Nagai T, Morino I, Yamazaki A, Deushi M, Yumimoto K, Maki T, Tanaka TY, Akaho T, Okumura H, Arai K, Nakatsuru T, Matsunaga T, Yokota T (2017) Lidar detection of high concentrations of ozone aerosol transported from northeastern Asia over Saga, Japan. *Atmos Chem Phys* 17:1865–1879. <https://doi.org/10.5194/acp-17-1865-2017>
- Van der Tol C, Verhoef W, Timmermans J, Verhoef A, Su Z (2009) An integrated model of soil-canopy spectral radiances, photosynthesis, fluorescence, temperature energy balance. *Biogeosci* 6:3109–3129
- Vapnik V, Lerner A (1963) Pattern recognition using generalized portrait method. *Auto Remo Cont* 24:774–780
- Walther S, Voigt M, Thum T, Gonsamo A, Zhang Y, Köhler JM, Varlagin A, Guanter L (2016) Satellite chlorophyll fluorescence measurements reveal large-scale decoupling of photosynthesis and greenness dynamics in boreal evergreen forests. *Glob Change Bio* 22:2979–2996
- White JD, Running SW, Nemani R, Keane RE, Ryan KC (1997) Measurement and remote sensing of LAI in Rocky Mountain montane ecosystems. *Can J For Res* 27:1714–1727
- Wilson EL, McLinden ML, Miller JH, Allen GR, Ott LE, Melroy HR, Clarke GB (2014) Miniaturized laser heterodyne radiometer for measurements of CO₂ in the atmospheric column. *Appl Phys B Lasers Opt* 114:385–393. <https://doi.org/10.1007/s00340-013-5531-1>
- World Data Center for Greenhouse Gases (2022) <https://gaw.kishou.go.jp/>. Accessed 29 Sept 2022
- World Health Organization (2016) Ambient air pollution-A global assessment of exposure and burden of disease. World Health Organization, Geneva
- Wunch D, Toon GC, Wennberg PO, Wofsy SC, Stephens BB, Fischer ML, Uchino O, Abshire JB, Bernath P, Biraud SC, Blavier J-FL, Boone C, Bowman KP, Browell EV, Campos T, Connor BJ, Daube BC, Deutscher NM, Diao M, Elkins JW, Gerbig C, Gottlieb E, Griffith DWT, Hurst DF, Jiménez R, Keppel-Aleks G, Kort EA, Macatangay R, Machida T, Matsueda H, Moore

- F, Morino I, Park S, Robinson J, Roehl CM, Sawa Y, Sherlock V, Sweeney C, Tanaka T, Zondlo MA (2010) Calibration of the total carbon column observing network using aircraft profile data. *Atmos Meas Tech* 3:1351–1362. <https://doi.org/10.5194/amt-3-1351-2010>
- Wunch D, Toon GC, Blavier J-FL, Washenfelder RA, Notholt J, Connor BJ, Griffith DWT, Sherlock V, Wennberg PO (2011a) The total carbon column observing network. *Philos Trans R Soc A* 369:2087–2112. <https://doi.org/10.1098/rsta.2010.0240>
- Wunch D, Wennberg PO, Toon GC, Connor BJ, Fisher B, Osterman GB, Frankenberg C, Mandrake L, O'Dell C, Ahonen P, Biraud SC, Castano R, Cressie N, Crisp D, Deutscher NM, Eldering A, Fisher ML, Griffith DWT, Gunson M, Heikkinen P, Keppel-Aleks G, Kyrö E, Lindenmaier R, Macatangay R, Mendonca J, Messerschmidt J, Miller CE, Morino I, Notholt J, Oyafuso FA, Rettinger M, Robinson J, Roehl CM, Salawitch RJ, Sherlock V, Strong K, Sussmann R, Tanaka T, Thompson DR, Uchino O, Warneke T, Wofsy SC (2011) A method for evaluating bias in global measurements of CO₂ total columns from space. *Atmos Chem Phys* 11:12317–12337. <https://doi.org/10.5194/acp-11-12317-2011b>
- Xiong X, Barnett C, Maddy E, Sweeney C, Liu X, Zhou L, Goldberg M (2008) Characterization and validation of methane products from the Atmospheric Infrared Sounder (AIRS). *J Geophys Res* 113:G00A01. <https://doi.org/10.1029/2007JG000500>
- Yoshida Y, Ota Y, Eguchi N, Kikuchi N, Nobuta K, Tran H, Morino I, Yokota T (2011) Retrieval algorithm for CO₂ and CH₄ column abundances from short-wavelength infrared spectral observations by the Greenhouse gases observing satellite. *Atmos Meas Tech* 4:717–734. <https://doi.org/10.5194/amt-4-717-2011>
- Yoshida Y, Kikuchi N, Morino I, Uchino O, Oshchepkov S, Bril A, Saeki T, Schutgens N, Toon GC, Wunch W, Roehl CM, Wennberg PO, Griffith DWT, Deutscher NM, Warneke T, Notholt J, Robinson J, Sherlock V, Connor B, Rettinger M, Sussmann R, Ahonen P, Heikkinen P, Kyrö E, Mendonca J, Strong K, Hase F, Dohe S, Yokota T (2013) Improvement of the retrieval algorithm for GOSAT SWIR XCO₂ and XCH₄ and their validation using TCCON data. *Atmos Meas Tech* 6:1533–1547. <https://doi.org/10.5194/amt-6-1533-2013>
- Zhang Y, Guanter L, Berry JA, Joiner J, van der Tol C, Huete A, Gitelson A, Voigt M, Köhler P (2014) Estimation of vegetation photosynthetic capacity from space-based measurements of chlorophyll fluorescence for terrestrial biosphere models. *Global Change Biol* 20:3727–3742

Publisher's Note

Springer Nature remains neutral with regard to jurisdictional claims in published maps and institutional affiliations.

Ryoichi Imasu is the chief scientist of the GOSAT-2 Science Team. TM is the project leader of GOSAT-2 in the National Institute for Environmental Studies (NIES). MN is the project manager of GOSAT-2 mission in Japan Aerospace Exploration Agency (JAXA).

Submit your manuscript to a SpringerOpen® journal and benefit from:

- Convenient online submission
- Rigorous peer review
- Open access: articles freely available online
- High visibility within the field
- Retaining the copyright to your article

Submit your next manuscript at ► [springeropen.com](https://www.springeropen.com)
